TÉCNICO LISBOA

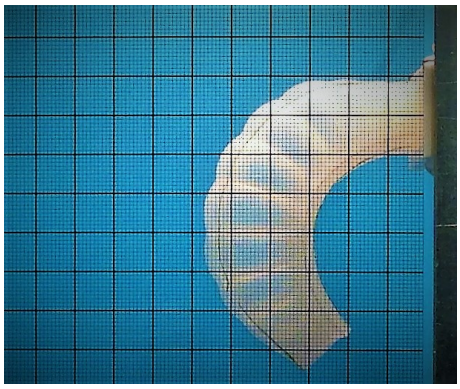

Sensing Pneu-net Devices Using Adaptive Materials

Vasco López Macedo de Soveral Rodrigues

Thesis to obtain the Master of Science Degree in

Mechanical Engineering

Supervisors: Prof. João Carlos Prata dos Reis
Prof. Paulo José da Costa Branco

Examination Committee

Chairperson: Prof. Paulo Jorge Coelho Ramalho Oliveira
Supervisor: Prof. João Carlos Prata dos Reis
Member of the Committee: Prof. Jorge Manuel Mateus Martins

June 2017

Basic research is what I'm doing when I don't know what I'm doing.

Wernher von Braun

Acknowledgments

I would like to thank Prof. João Reis and Prof. Paulo Branco for guiding me through this thesis and sharing their wisdom and experience. I would also like to thank my friends and colleagues, with whom I frequently shared thoughts and discussed relevant ideas for my thesis, namely João Oliveira, Pedro Pontes, Catarina Carvalheiras, Henrique Carvalho, Ricardo Pacheco and Francisco Lemos.

Abstract

The continuous deformation properties of soft actuators have created a need for the application of equally compliant sensors. In this work, the use of an IPMC material as a sensor is studied for curvature feedback in a soft pneu-net actuator.

For improving the sensor response, electrolytes with propylene carbonate and Li^+ counter-ions in different concentrations were tested in IPMC samples. It was found that a solute concentration of 15 g/l allowed for the highest amplitude in the response signal from all the tested concentrations. A sample with this electrolyte was used for estimating a linear dynamic model, describing its electrical response to imposed curvature.

A sensor encapsulation method using silicone was developed, allowing for its direct integration in the pneu-net actuator structure. The final instrumented actuator was tested and its sensor feedback validated, demonstrating the feasibility of the developed approach. It was found that certain characteristics of the sensor hampered its application in conditions where either long duration static bending or very slow movements were to be measured. Nevertheless, for use cases where cyclic or transient bending is to be detected, this type of sensor presented a viable option for application in soft robots.

Keywords

IPMC, Pneu-net, Soft Robotics, Adaptive Materials, Inflatable Actuator

Resumo

As características de deformação contínua existentes em atuadores construídos em materiais macios originaram uma necessidade de aplicação de sensores igualmente complacentes. Neste trabalho, o uso de um material eletroativo IPMC como sensor é estudado para efeitos de deteção de curvatura num atuador do tipo pneu-net.

De modo a melhorar a resposta do sensor, testaram-se amostras de IPMC com eletrólitos de carbonato de propileno e iões Li^+ em diferentes concentrações. Verificou-se que uma concentração de 15 g/l de soluto originou uma resposta de maior amplitude do que todas as outras testadas. A partir de uma amostra com esta concentração foi estimado um modelo dinâmico linear, para caracterizar a resposta elétrica a uma curvatura imposta.

Foi desenvolvido um método de encapsulamento do sensor com silicone, que permitiu a sua integração direta na estrutura do atuador pneu-net. O actuador com sensor de curvatura integrado foi testado e a resposta do sensor foi validada, demonstrando assim a sua viabilidade. Verificou-se que o sensor possuía características que dificultavam a sua aplicação em situações nas quais se pretendesse medir deformações muito lentas ou estáticas durante longos períodos de tempo. No entanto, para casos em que a deteção de flexão cíclica ou transiente seja desejável, este sensor demonstrou ser uma opção adequada para aplicações em robôs com materiais macios.

Palavras Chave

IPMC, Pneu-net, Robôs com Materiais Macios, Materiais Adaptativos, Atuador Insuflável

Contents

List of Figures

List of Tables

Abbreviations

IPMC - Ionic Polymer-Metal Composite
Pneu-net - Pneumatic Network (class of soft actuator)
PZT - Lead Zirconate Titanate (ceramic piezoelectric material)
SPA - Soft Pneumatic Actuator
EAP - Electroactive Polymer
OpAmp - Operational Amplifier
PLA - Polylactic Acid
LED - Light-Emitting Diode
IIR - Infinite Impulse Response
fft - Fast Fourier Transform
FIR - Finite Impulse Response
FEA - Finite Element Analysis

List of Symbols

Roman symbols

i	Electrical Current
R_{dif}	Equivalent IPMC resistance
I_{mec}	Electrical current related to mechanical deformation of an IPMC
C_{ext}	Equivalent IPMC capacitance
l	IPMC width
L_p	Parameter depending on ion mass and charge density
G	Shear Modulus
x_1	Dimension along the IPMC length
E	Young's Modulus
d	IPMC thickness
k	Curvature
$K(s)$	Laplace transform of curvature
$V(s)$	Laplace transform of voltage
R_d	Shunt Resistor
r_{mec}	Mechanical parameter, dependent on the shear modulus, Poisson coefficient and the geometry of the IPMC
W	Strain energy density function
N	Ogden model order
D_1, D_2, D_3	Ogden model parameters
X	Cartesian coordinate
K_{amp}	Amplifier gain
k_i	measured curvature
R_i	mid-thickness radius
$G(s)$	First-order derivative model transfer function
$H(s)$	Empirical IPMC transfer function
a	value of the system pole
$J(s)$	Inverse empirical IPMC transfer function

Greek symbols

λ	Elastic constant
ν	Poisson's Coefficient
ξ	Transverse displacement of the neutral plane
$\lambda_1, \lambda_2, \lambda_3$	Principal stretches
μ_1, μ_2, μ_3	Ogden model parameters
μ_p	Ogden model coefficient
$\alpha_1, \alpha_2, \alpha_3$	Ogden model parameters
α_p	Ogden model coefficient

1 Introduction

1.1 Motivation

A rising trend in robotics has been the focus on compliant devices able to interact safely with humans. Soft robots present advantages in this area, due to their inherent compliance, which is not limited by control bandwidth. Usually, this class of robots has the capability to achieve continuous deformation, enabling the emulation of biological systems. Also, they can be made to withstand large shape changes, being able to fit in narrow spaces or deform around objects.

Completely soft robots cannot usually be actuated using traditional mechanisms involving motors connected to joints. A type of mechanism that has proven particularly suitable for these applications is pneumatic actuation. Soft pneumatic actuators can be embedded within the soft structure of the robots, providing continuous deformations without requiring rigid components in the actuated zones.

Due to the complex shapes attained by these structures and its continuous nature, traditional sensors used for stiff mechanisms cannot be used for position feedback. As such, equally soft sensors capable of deforming along with the robot and measuring local curvature would be desirable, to allow for feedback control strategies to be implemented.

With this in mind, it was decided to explore the application of electro-active ionic polymer-metal composites (IPMC) as flexible curvature sensors, directly embedded in the soft actuator structure. Since an encapsulation has been suggested for improving the longevity and performance of these materials, it seemed an adequate application to include them inside the silicone structure of a pneu-net device.

1.2 State of The Art

1.2.1 Soft Robotics

The field of Soft Robotics is focused on the study of compliant structures and actuators capable of continuous deformation. Soft robotic structures have shown advantages for applications involving human-robot interaction [1] or manipulation of complex objects [2], where compliance is seen as a more valuable characteristic than precision. These robots are usually able to provide an intrinsically safe interaction without requiring complex control and actuation systems.

The inclusion of continuously deformable actuators allowed for the development of biologically-inspired robots, including soft swimming-capable robotic fish [3] and [4] and the soft limbs of invertebrate animals, such as tentacles [5].

Pneumatic actuation is one of the most used methods for producing motion in soft robots. Soft pneumatic structures have been used as grippers [6], robotic manipulators [1] and even standalone mobile robots [7].

Historical Perspective and Recent Developments

In 1976, a patent was granted for the *Simrit Finger* [8], a bellows-type actuator capable of controlled bending motion. The device was made of a polymeric material and had a hollow semi-circular cross-section. Its walls had corrugations that extended partially around the section perimeter, allowing for asymmetrical deformation when the interior chamber was pressurized. The mechanics of this type of actuator were studied by Wilson, and various robotic applications were devised [9]. These include robotic arm, using five Simrit Finger bending actuators connected in series to make the arm structure and two in parallel for the gripper. Using an open-loop control method, it was reported to have achieved a positional error of no more than nine percent, during a benchmark pick-and-place maneuver.

Figure 1.1: Bellows robotic arm [10].

Recently, a new generation of pneumatic actuators has received increased attention in research. Known as Soft Pneumatic Actuators (SPA), these are made of soft and stretchable materials such as silicone-rubber, and may also combine stiffer or nearly inextensible materials to help achieve the desired motion profile. Bending actuators made almost entirely of silicone, using a series of connected air chambers on top of a nearly-inextensible material layer were developed by [6]. These are commonly called pneu-net (Pneumatic Network) actuators, and have the advantage of being highly customizable and easy to manufacture, besides its inherent compliance properties (figure 1.2).

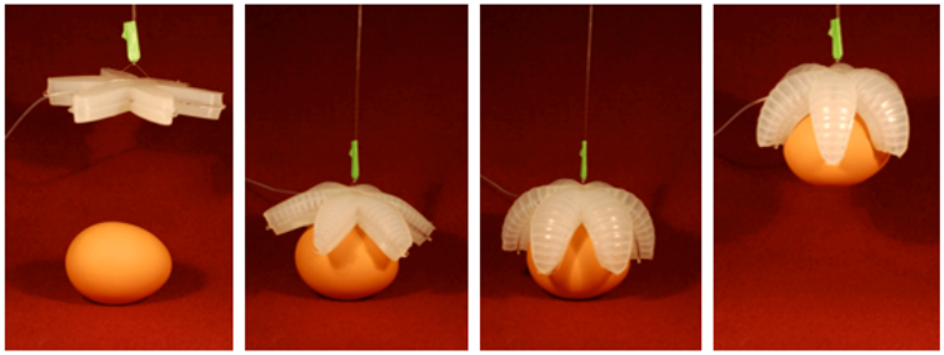

Figure 1.2: Pneu-net gripper handling an uncooked chicken egg [6].

A characterization of such actuators was made by Yi Sun *et al.* [11], where the force and torque outputs of actuators with different geometries were analyzed and a physical model was presented.

In order to overcome the speed limitations of conventional SPAs, a new geometry was proposed by Mosadegh *et al*. [12], which reduces the volume of air, as well as the pressure, required to achieve a certain deformation with a soft bending actuator. By separating the transversal and upper chamber walls, the strain in the upper and lateral walls is reduced, thereby decreasing the bending resistance of the structure in the actuated direction. This increases the amount of useful work (i.e. in the desired direction) made by the pressurized air inside the chambers.

In parallel, reinforced soft pneumatic actuators have also been explored. These have used higher stiffness, nearly inextensible or orthotropic materials to reinforce the chamber walls and achieve the desired mechanical properties. Examples of such actuators include reinforcements with paper [13] and aligned fibers [14]. These devices usually allow for stronger actuation forces without excessive strain in the chamber walls, but are more complex to manufacture, due to the integration of the reinforced material inside the silicone structure.

Challenges

In order to master the design of capable soft robots, a number of challenges need to be overcome:

- Due to its continuous deformation capabilities, unconventional materials need to be explored.
- Fabrication methods for soft robots are much less developed than those for their rigid counterparts. The soft nature of the materials used does not allow most conventional subtractive manufacturing to be used.

- Because of the large deformations that can occur in these structures and the nonlinear properties of its materials, simple linear models do not accurately describe its mechanical behavior. This requires more advanced modeling and simulation techniques - a developing research topic in soft robotics.

1.2.2 IPMC Materials

Electroactive polymers (EAPs) are polymer materials whose shape or dimensions change when an electrical field is applied. These properties were studied as early as 1880, by Röntgen [15]. Since the mid-1970s, EAPs became the subject of many research activities, and applications of these materials as alternatives for conventional actuators or as compliant sensors began to be studied [16].

Characteristics of IPMC Materials

Ionic polymer metal composites (IPMC) are a specific type of electroactive materials, which has been recently studied for use in ”artificial muscles” and initially applied in biomimetic flexible robots.

These composites consist of a fine polymeric membrane, coated with a noble metal (usually Ag or Pt) on both sides (figure 1.3). The membrane is made of an ionomer, a polymer containing a fraction of ionized repeat units covalently bonded to its backbone structure. This characteristic allows for selective ion permeability. Usually, Nafion® or Flemion ®, both developed by DuPont, are used as membrane ionomers in IPMC materials. In the case of Nafion, the polymer backbone is composed of a terafluorethylene (Teflon), with perfluorovinyl ether groups terminated with negatively charged sulfonate groups (SO_3^-). When immersed in an electrolyte solution - containing positive and negative ions - the membrane will conduct the cations, while being impermeable to anions. Due to its ionomer properties, this type of polymer has been used in fuel cells, as a proton-exchange membrane [17].

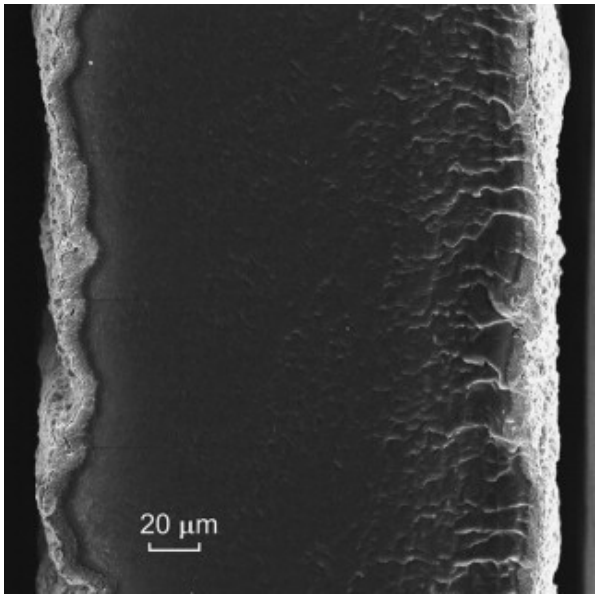

Figure 1.3: IPMC cross-section , showing noble metal electrodes on both sides [18].

IPMC materials are capable of producing large bending deformations, when an electric field is ap-

plied between the electrodes (figure 1.4). Conversely, when a mechanical deformation is induced in the polymer, a differential voltage will be generated at both sides of the material. Although the underlying mechanism is different, these properties show similarities with those of piezoelectric materials.

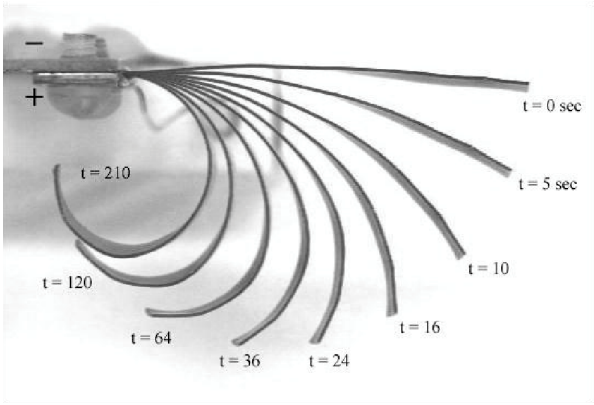

Figure 1.4: Successive photos of a bending IPMC [19].

Compared to the PZT piezoelectric material (Lead Zirconate Titanate), IPMCs are able to undergo large bending deformations with low applied voltages (in the order of 2 volts), while the former are only able to produce very small displacements, usually with much higher voltages [20]. On the other hand, piezoelectric materials are able to produce larger forces than IPMCs, and do not require an electrolyte for proper operation as an actuator. Table 1.1 shows the main differences between these electroactive materials.

Table 1.1: Characteristics of IPMC versus PZT, adapted from [20].

Material	IPMC	PZT
Voltage	0.5 — 3.0 V	50 — 300 V
Deformation	mm	μm
Force	mN	N
Mechanical Properties	• Elastic and flexible material with an elastic modulus of 0.18 GPa; • Effective mass density of 3000 Kg m^{-3}.	• Rigid and fragile, with an elastic modulus of 80 GPa; • Mass density of 7700 Kg m^3

In 2000, two separate investigation groups, led by Tadokoro [21] in Japan and P. G. De Gennes [22] in the United States of America, studied and presented the first theoretical and experimental results on the electroactive characteristics of IPMC materials. It was shown that, when subjected to an electrical field, these materials developed internal forces capable of deforming its structure.

Various techniques for the addition of a metallic outer layer to the ion-exchange polymer have been used. Examples of such methods are reported in [16], including reducing reactions, physical metal loading, casting, hot-pressing and electroless plating. The metal electrodes on each side of the ionomer membrane must be porous, in order to allow the passage of positive ions from the electrolyte to the polymer. The surface of these electrodes has been reported to have small cracks [23], which

may affect the stiffness of the composite, as well as electrolyte mobility.

In order to improve its electromechanical response, IPMC devices are usually immersed in a suitable electrolyte, comprising a polar solvent and a salt. The most commonly used counter-ion is Na+, but electrolytes with Li^+, TEA^+ (tetraethylammonium) and Cs+ have also been tested [19, 24]. It has been shown that the behavior of IPMCs changes depending on the counter-ions used. Electrolytes with Li^+ have been shown to increase the actuator performance when compared to Na^+, allowing for larger bending deflections [24].

IPMC Modelling Attempts

Although various physical models for describing the electromechanical behavior of IPMCs have been proposed, their relevant physical phenomena are not yet fully understood.

One of the first models derived at a microscopic scale was proposed by Shahinpoor [25], considering only the forces induced by an electric field on the fixed anions and mobile cations. Due to its microscopic nature, difficulties have been encountered in the determination of its parameters.

In 2000, Tadokoro proposed in [26] that the bending motion of the IPMC was caused by the differential swelling inside the ionomer structure, which would cause contraction and expansion along its thickness. During the application of an electric field, the water molecules would be dragged by moving cations, causing its redistribution.

A complete physical model was also proposed in 2000 by Nemat-Nasser [27], based on the redistribution of cations inside the IPMC structure. Ionic clusters would form in the negatively-charged polymer side chains, where water molecules and cations would be accumulated. When applying an electric field, a locally imbalanced charge density would induce stresses in the backbone polymer, causing its deformation. This model initially accounted only for the effect of electrostatic forces, but a later revision included the effects of water migration inside the polymer [28].

Based on previous work developed by Shahinpoor and Nemat-Nasser, a new model was presented by Branco and Dente in [29], derived on a macroscopic level and based on continuum electromechanical concepts. This model allowed for an equivalent, lumped-parameter, electrical circuit representation. For explaining the IPMC motion, the effects of mobile anions were included, while those of water migration were neglected. Simulations of this model were validated with experimental results.

1.3 Main Contributions

In this dissertation, a number of contributions are made, regarding the study of an adaptive IPMC sensor and its application in soft robotics. These include:

- Testing of an IPMC in sensor mode with a Propylene Carbonate and Li Salt electrolyte in various concentrations, to assess the effects of this parameter in the sensing performance.
- Acquisition of useful data for modeling the sensor, from step response and low-frequency oscillation tests done with a silicone encapsulation.

- Testing of new encapsulation methods for IPMC strips, using a soft silicone and specially-designed molds.
- Integration of an IPMC sensor in a pneu-net actuator, for curvature feedback.

1.4 Thesis Outline

In this chapter, the concept behind this thesis and its motivation were described, along with a review of the relevant developments in the areas of soft robotics and IPMC materials. The coming chapters will further develop these ideas, in the following structure:

- Chapter 2 will describe a theoretical model for the electromechanical response of IPMCs, as well as the method used for modeling the mechanical behavior of the proposed soft actuator;
- Chapter 3 will focus on the experiments devised for testing the IPMC as a sensor, the characteristics of the prototypes built and the manufacturing techniques used;
- In Chapter 4, results from the sensor identification experiments will be presented and discussed, along with a validation of the modeling methods used. A final instrumented actuator prototype will be presented and its sensing performance validated.
- Lastly, in Chapter 5, conclusions made regarding the tested methods, their advantages and limitations will be described.

2

Theoretical Background and Modelling

A theoretical model describing the electromechanical properties of IPMC materials and the mechanical properties of silicone is presented, and a finite element model of the benchmark actuator is described.

2.1 Physical Model of an IPMC Sensor

As briefly described in section 1.2.2 , the physical model by Branco and Dente [29] should allow for a prediction of the IPMC response based on macroscopic physical variables. This equivalent lumped-parameter model was used in this work for comparison with an estimated empirical model, to be presented in section 4.1.7.

An equivalent electrical circuit representation, seen in figure 2.1, of the model mentioned above can be described by the following equation:

$$i = \frac{1}{R_{dif}} V + I_{mec} + C_{ext} \frac{\mathrm{d}V}{\mathrm{d}t} \tag{2.1}$$

where R_{dif} is an equivalent resistance and C_{ext} is an equivalent capacitance. I_{mec} is an electrical current related to mechanical deformation and defined in [29] by

$$I_{mec} = l L_p \left[\int_0^b \left((2G + \lambda(\nu - 1)) \frac{\partial^2 \xi}{\partial x_1^2} \right) \mathrm{d}x_1 + Y \frac{d^2}{12} \int_0^b \frac{\partial^4 \xi}{\partial \xi^4} \mathrm{d}x_1 \right] \tag{2.2}$$

where l is the width of the IPMC, L_p is a parameter depending on ion mass and charge density, G is the shear modulus of rigidity, λ is an elastic constant, ξ is the transverse displacement of the neutral

plane, x_1 is the dimension along the IPMC length, Y is the Young's modulus and d is the thickness of the IPMC.

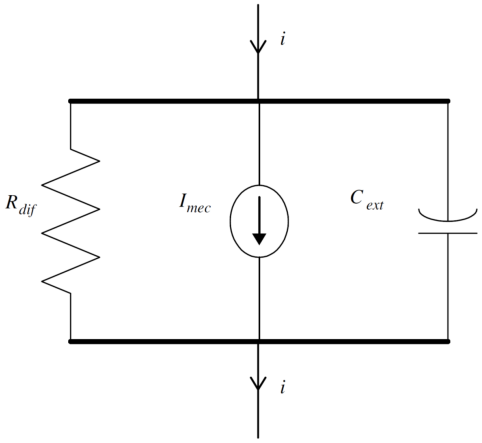

Figure 2.1: Equivalent circuit representation of an IPMC [29].

Assuming a uniform curvature over the length of the IPMC, the partial derivatives of the transverse displacement simplify to $\frac{\partial^2 \xi}{\partial x_1^2} = k$ and $\frac{\partial^4 \xi}{\partial \xi^4} = 0$, where k is the curvature value. The expression for I_{mec} is therefore reduced to

$$I_{mec} = lL_p k \int_0^b \Big(2G + \lambda(\nu - 1)\Big) \mathrm{d}x_1 \tag{2.3}$$

Connecting both sides of the IPMC with a shunt resistor, as shown in figure 2.2, the current i becomes related to the voltage V, by

$$i = \frac{V}{R_d} \tag{2.4}$$

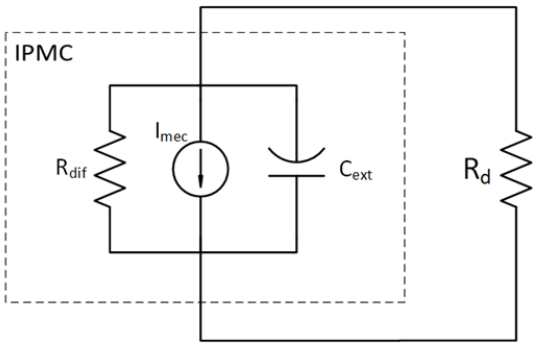

Figure 2.2: Equivalent circuit representation of an IPMC with a shunt resistor R_d connected to the electrodes.

Assuming only parameters V, i and k can change with time, equation 2.1 can be rewritten as

$$\left(\frac{1}{R_d} - \frac{1}{R_{dif}}\right) V(t) - C_{ext} \frac{\mathrm{d}V}{\mathrm{d}t} = L_p r_{mec} k(t) \tag{2.5}$$

where r_{mec} is a mechanical parameter, dependent on the shear modulus G, Poisson coefficient ν and the geometry of the IPMC.

Applying the Laplace transform on both sides of equation 2.5 and rearranging, a transfer function from the curvature to the output voltage of the IPMC can be obtained:

$$\frac{V(s)}{K(s)} = \frac{L_p \frac{r_{mec}}{C_{ext}}}{s - \frac{R_{dif} - R_d}{R_{dif} R_d C_{ext}}} \tag{2.6}$$

The expression above represents a first-order linear time-invariant model, describing the relationship between the curvature of the IPMC and the output voltage measured between the terminals of resistor R_d.

2.2 Modelling of a Pneu-net Actuator

2.2.1 Material Models

In order to perform a finite element analysis of a pneu-net actuator, suitable models should be chosen for describing the properties of its materials.

The chosen material for building the actuator body was Ecoflex® 00-30 , a very soft silicone produced by Smooth-On, Inc., which can be cured at normal temperatures and is reported to withstand strains in excess of 600% before failure [30]. For large deformations, such as those that are present in the actuator when its chambers are pressurized, the stress-strain relationship for this kind of material is not accurately described by a simple linear function such as Hooke's Law. Therefore, a hyperelastic model is used, describing a nonlinear behavior in the elastic regime.

From the available hyperelastic models, a 3rd-order Ogden model was chosen, using the parameters identified by Agarwal *et al.* [31] for the Ecoflex®00-30 material. The strain energy density function for this type of model is given by

$$W(\lambda_1, \lambda_2, \lambda_3) = \sum_{p=1}^{N} \frac{\mu_p}{\alpha_p} (\lambda_1^{\alpha_p} + \lambda_2^{\alpha_p} + \lambda_3^{\alpha_p}) \tag{2.7}$$

where λ_1, λ_2 and λ_3 are the principal stretches, N is the model order and μ_p and α_p are coefficients that depend on the material. The parameters identified for Ecoflex® 00-30 in [31] and shown in table 2.1 were used.

Table 2.1: Ogden model parameters for Ecoflex® 00-30

Parameter	Value
N	3
α_1	-3.848
α_2	0.663
α_3	4.225
μ_1	0.001887
μ_2	0.02225
μ_3	0.003574
D_1	2.93
D_2	0
D_3	0

2.2.2 Benchmark Actuator Characteristics

The benchmark actuator geometry was based on a previously developed design, inspired by [6]. It has the approximate size of a human finger, which can be easily integrated in a soft gripper for robotic applications.

The finger-like actuator has 10 communicating air chambers, connected to an attached rubber air tube at the base. It has a rounded tip and straight walls, maintaining a constant width and height along its length. All the chambers have the same dimensions.

A strain-limiting layer, located 3 mm above the lower face of the pneu-net body and 3 mm below the air chambers, covered all the length and width of the actuator. The material chosen was a cotton textile with approximately one thread per millimeter.

The relatively simple geometry, shown in figure 2.3, was advantageous both for manufacturing and for the initial simulation attempts, as it could easily be covered by a regular mesh.

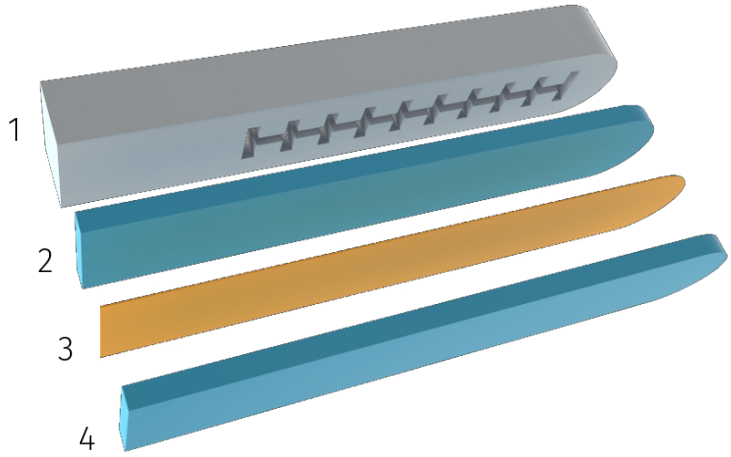

Figure 2.3: Exploded view of the benchmark pneu-net: 1 - Main body with air chambers; 2 and 4 - silicone base layers; 3 - strain-limiting layer

2.2.3 Elements and Mesh

A finite element analysis of the benchmark actuator was performed, following a similar approach to the one suggested in [32].

The solid-body geometry of the actuator was covered by a three-dimensional structured mesh, generated using Abaqus CAE. For that purpose, 10-node tetrahedral elements were used, with quadratic interpolation. The extensible layer was represented by a 2D mesh of triangular membrane elements with 7 nodes, also using quadratic interpolation.

A hybrid formulation was chosen for the three-dimensional elements, to allow for the nearly-incompressible behavior of silicone to be simulated, reducing the effects of volumetric locking.

Due to the symmetric properties of the actuator body, only half of the geometry was modeled for the finite element analysis. This required an additional (symmetry) boundary condition, but had the advantage of reducing the mesh size while also exposing the interior of the air chambers and the wall section directly in the results.

For the initial simulations, a mesh was generated with global seeds. A value of 2.8 mm for the approximate global size of the elements was found to be adequate for covering the geometry without irregularities, as shown in figure 2.4. Although this mesh allowed for quick simulation runs without errors when moderate pressures were applied, it did not provide a good resolution for identifying stress concentration zones or chamber wall curvature. Also, for initial test simulations with higher pressures, causing the actuator to reach angles above 90º between the tip and the base and greater strains in the chamber walls, some elements were found to have excessive distortion.

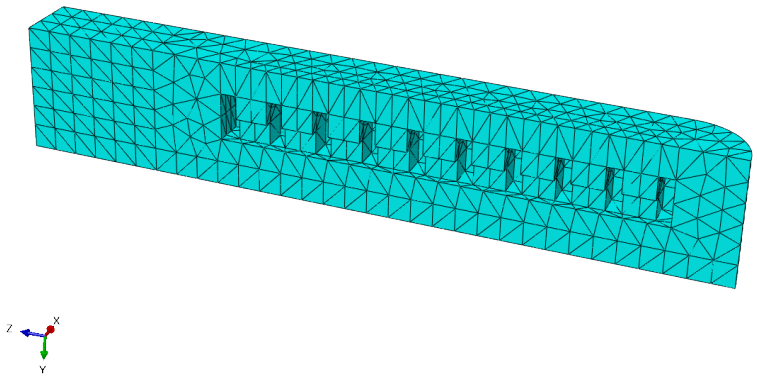

Figure 2.4: Initial mesh generated with global seeds.

Based on a first analysis of the mesh in deformed conditions, a modified mesh was generated using local seeds in the chamber edges, and through the thickness of the upper chamber walls. This configuration, represented in figure 2.5, reduced distortion on the vertical chamber walls that stretch upwards, by slightly changing the aspect ratio of the elements and increasing the number of vertical divisions. The same technique was applied to the top chamber walls, greatly increasing the number of subdivisions in the horizontal dimensions.

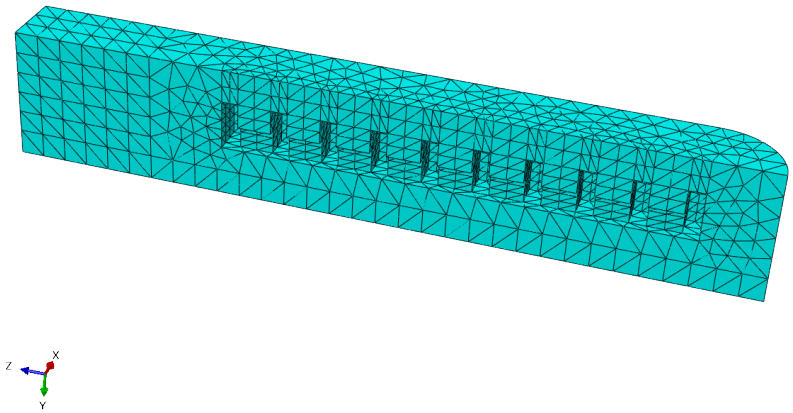

Figure 2.5: Improved mesh with local seeds.

The inextensible layer was modeled with membrane elements, which have the traction and compression properties found in a shell element, but without bending stiffness. This way, a simple isotropic

approximation of the macroscopic behavior of a textile can be modeled, representing the textile fabric layer in the real actuator.

2.2.4 Loads and Boundary Conditions

For the purpose of validating the finite element model of the benchmark actuator, several load cases were tested in the real prototype and the same conditions were then applied to the simulation.

In the first load case, only gravity was applied to the body. The pressure differential between the inside and outside of the pneumatic chambers was therefore null. This allowed for a confirmation of the material density properties, as well as the stiffness in low stress conditions.

For the next load cases, the pressure was gradually increased, in conformity with the values tested in the real prototype. For very high deflections, where the actuator tip would be at an angle above 90^o to the horizontal plane, high distortions and irregular displacement behavior were detected on the mesh, next to the regions where fixed-displacement boundary conditions were applied. For this reason, the simulated model was not validated for higher deflections.

The pressure loads applied to the finite element model for validation purposes have the same values as those measured during tests with the benchmark pneu-net prototype. These are displayed in Table 2.2.

Table 2.2: Finite element analysis pressure loads.

Test	Pressure Load [kPa]
1	0
2	21.5
3	25.5
4	28.5
5	29
6	29.9

Two different boundary conditions were applied in the model: a zero-displacement constraint at the base of the actuator geometry and a symmetry constraint at the cutting plane.

The zero-displacement constraint, shown in figure 2.6, represents a slightly simplified version of the interface with the fixed encasing of the real prototype. The small grooves that exist in that region of the prototype were not modeled. After the gravity load step, an additional fixed-displacement condition was added in the chamber wall closest to the encasing, as an approximation to the high stiffness provided by the rubber tube end. This prevented the chamber from expanding in the direction of the encasing, and was verified to lead to better results, during the initial comparisons between the prototype and the finite element model.

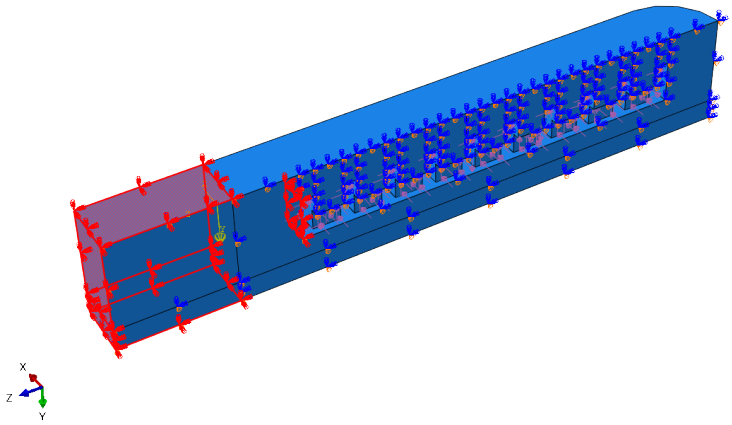

Figure 2.6: Zero-displacement boundary condition, applied to the regions highlighted in red.

The symmetry constraint (figure 2.7) fixed the displacement of the nodes in the cutting plane along the X direction. This allowed for the simulation of the whole actuator body using half of the geometry and thus half of the elements.

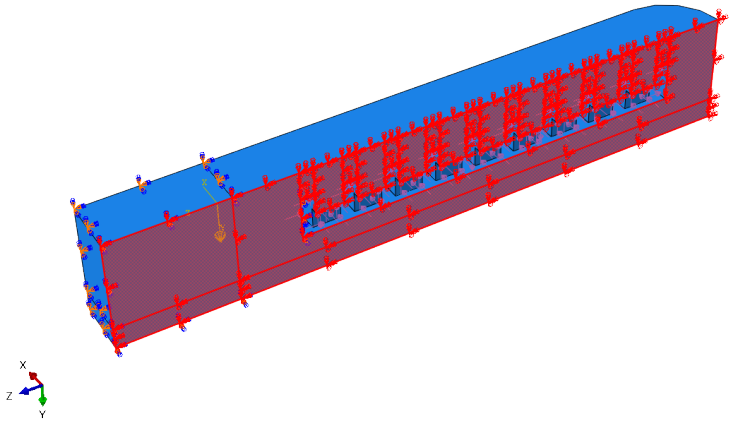

Figure 2.7: Symmetry boundary condition, applied to the regions highlighted in red.

2.2.5 IPMC inclusion in the finite element model

To predict the effects of the IPMC sensor in the instrumented pneu-net actuator, the mechanical properties of the material were accounted for in the finite element model. For this purpose, a mesh with shell-type elements with the sensor geometry was introduced over the existing membrane mesh in the inextensible layer. Although in a real application there would be a small offset between the sensor and the inextensible layer, in this model, that distance is approximated to zero.

The IPMC layer was modeled in different locations of the actuator during preliminary simulations, before the configuration presented in 3.4.1 was defined.

3

Experimental Procedure and Prototypes

The encapsulated IPMC sensor characteristics and manufacturing methods are described. Experimental procedures for the IPMC characterization tests are shown. A benchmark soft actuator for finite-element model and manufacturing validation is presented, as well as the final sensing actuator prototype.

3.1 Encapsulated IPMC Sensor

Before testing, all IPMC samples were encapsulated to avoid electrolyte loss and also to better represent their final configuration in the pneumatic actuator. In order to ensure the electrolyte would not escape, it was decided that the samples would be covered by a soft material with a sufficiently low permeability to the electrolyte.

3.1.1 Encapsulation

Since Ecoflex® 00-30 was planned to be used as the primary material for the soft pneumatic actuator, it made sense to experiment with encapsulating the IPMC strips in the same material, facilitating their future inclusion in the actuator body and minimizing their influence on its mechanical behavior.

Two different methods were considered for encapsulating the sensor:

- Casting two separate halves of the final part and joining them with liquid silicone, leaving a middle slot for introducing the IPMC strip and contacts;
- Directly casting the whole encapsulation, using a mold specially designed to keep the IPMC strip aligned in a middle position.

Due to the electrolyte used in almost all sensor configurations to be tested, the copper contacts used could not be attached to the platinum layers using conductive glue, since it would be dissolved by the Propylene Carbonate solute. Also, due to difficult adhesion and the effects excessive heating in the ionomer membrane, the contacts were not soldered to the sensor. Instead, it was decided that the contacts would simply be pressed against the platinum surfaces and either the encapsulation itself or an external part would keep them in the correct position.

3.1.2 Type 1 Encapsulation

Built for the IPMC frequency tests, this encapsulation consisted of a parallelepiped-shaped silicone part with a slot at half thickness, in which an IPMC strip and contacts could be inserted (figure 3.1). After these were positioned, the external openings of the slot were sealed with a thin layer of silicone, thereby preventing the sensor, as well as the electrolyte, from exiting the encapsulation.

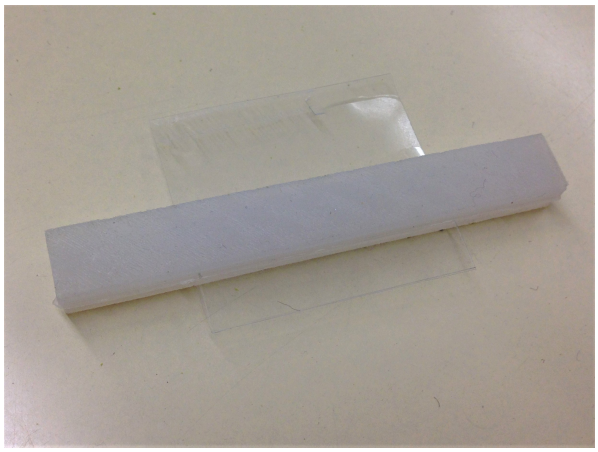

Figure 3.1: Two silicone parts being joined into a type 1 encapsulation. Note the plastic plate forming a slot for the IPMC.

Two flexible copper contacts, placed at half the strip length before sealing the slot, allowed the electrical connection to a signal conditioning and measurement circuit. For the connection to be maintained during the frequency test oscillations, an external component locally pushed the silicone over the contacts (figure 3.2).

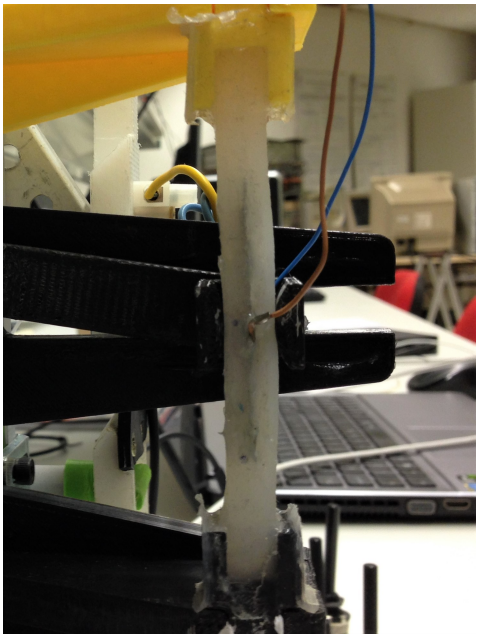

Figure 3.2: Type 1 encapsulated sensor mounted on an oscillation test bench. A plastic clamp is pressing the copper contacts against the IPMC.

3.1.3 Type 2 Encapsulation

While the type 1 encapsulation was successfully used for frequency testing, it still could not guarantee that no electrolyte would escape the interior of the ionomer membrane to the adjacent space inside the slot. Therefore, it was desirable to have a tight encapsulation that would stick to the platinum electrodes of the IPMC, eliminating the air gap that might exist around the sensor, following the idea described in [33].

The chosen solution was to insert the IPMC into the liquid silicone, before letting it cure with the strip and contacts directly embedded. To prevent the liquid silicone from covering the area between the contacts and the sensor, the former were pressed against the latter with constant force, during the curing process. The mold used for manufacturing, shown in figure 3.3, consisted of two different parts, each with two cylindrical protrusions for pressing the contacts and other features for alignment.

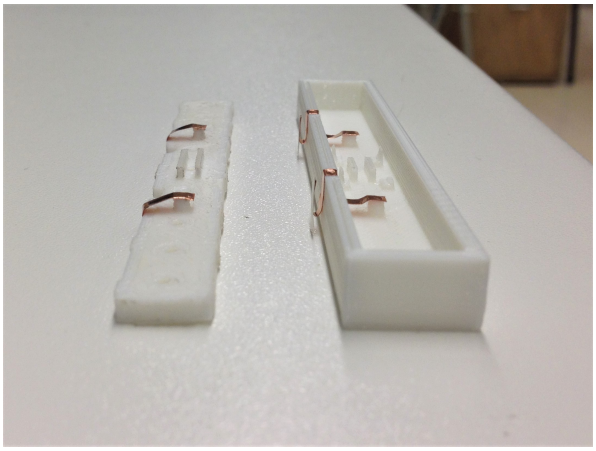

Figure 3.3: Type 2 encapsulation mold with inserted contacts.

Before placing the IPMC in the mold, its support and alignment surfaces were covered with a thin layer of silicone, on both parts. After curing the first silicone layer, the contacts were positioned on top of the cylinders, the IPMC was inserted and the two halves of the mold were compressed together with the help of rubber bands. Once this setup was completed, liquid silicone was injected in the mold through the openings available, using a syringe (figure 3.4).

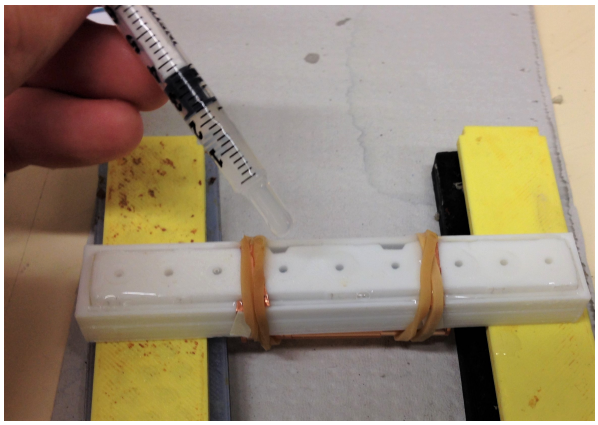

Figure 3.4: Injecting silicone into a Type 2 encapsulation mold.

After completing the curing process and removing the resulting piece from the mold, its imperfections were either cut or filled with liquid silicone, to obtain a smooth external surface, as seen in figure 3.5. The finished encapsulation was then bonded to two plastic fittings at its extremities, in order to be used in the test stand.

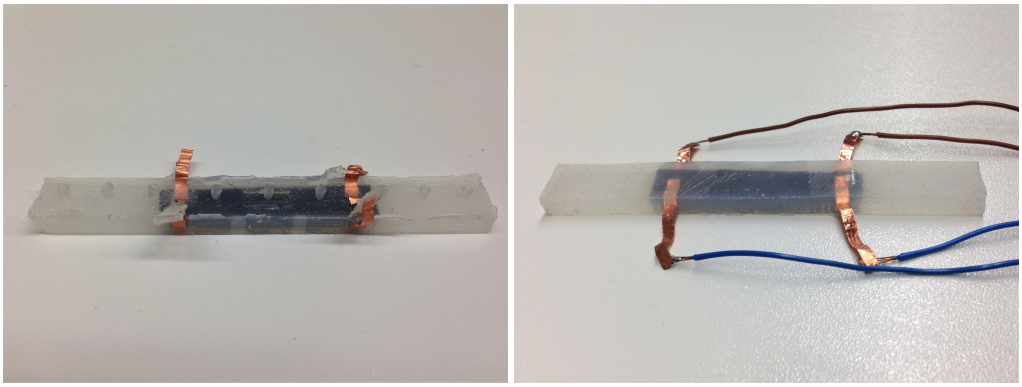

(a) Encapsulated sensor after curing.

(b) Encapsulated sensor with imperfections removed and wires soldered to the contacts.

Figure 3.5: Type 2 encapsulated sensor.

3.2 IPMC Sensor Identification

3.2.1 Introduction

For the empirical identification of a model for relating the electrical output of the IPMC sensor with the mechanical deformation, a controlled method of imposing displacement on the sensor was

devised.

The reported experiments were carried out in order to assess the influence of the electrolyte in the electrical response of a mechanically-stimulated IPMC sensor encapsulated in Ecoflex 0030. Secondly, the acquired data through oscillations at various frequencies allowed for a dynamic model to be fitted, describing the behavior of an IPMC sensor at low frequencies. Lastly, the experimental setup was used to validate the proposed encapsulation concepts.

3.2.2 Testing Equipment

In order to control the imposed displacement on the sensor and measure its output, a specialized test bench was built, with two different excitation mechanisms.

3.2.2.A Oscillating Mechanism

The first test for model identification and performance comparison involved cyclically bending the IPMC samples. For that purpose, an oscillating mechanism was built, based on the crank-and-slider concept. The system converted the rotational displacement of an electric motor shaft to linear displacement at the IPMC contact point.

The electric motor that moves the shaft is controlled using an attached hall-effect encoder and a transistor-based circuit connected to an Arduino UNO micro-controller board. The motor circuit, represented in figure 3.6, is connected to a 12V external power supply.

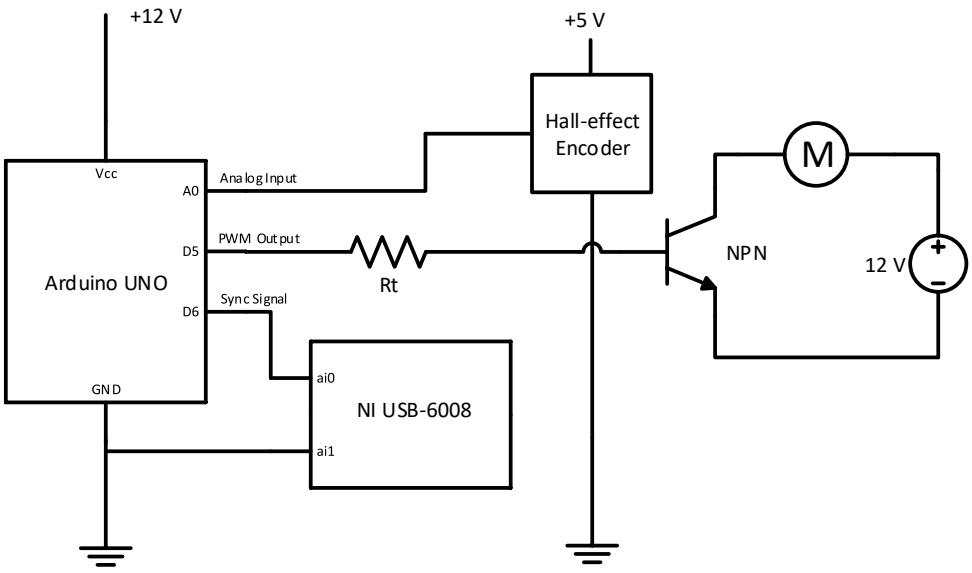

Figure 3.6: Motor control circuit for the oscillating mechanism.

The crank, connecting rod and sliding IPMC pusher were dimensioned for a total pusher displacement of 40 mm during operation. These parts, along with the rail, encapsulation fittings and supports,

were manufactured in PLA using a 3D printer. Figure 3.7 shows the assembled mechanism, with a mounted IPMC test sample.

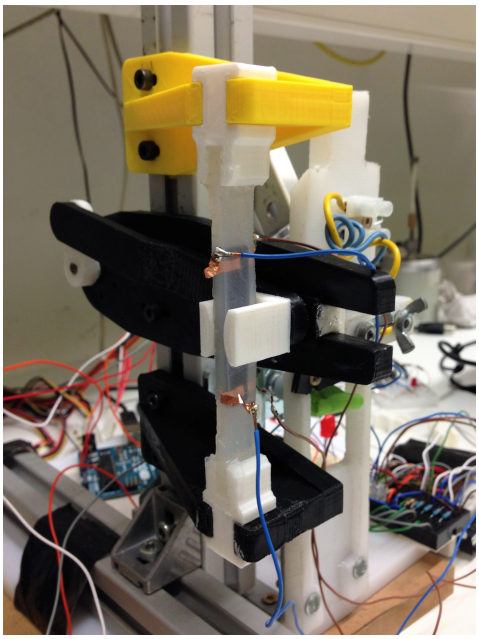

Figure 3.7: Assembled oscillating test bench.

To control the oscillation frequency of the slider, a velocity PID controller was implemented in the Arduino board. With the available hardware, the resulting frequency range available for reliable operation during experiments was found to be between 0.4Hz and 3Hz.

A MATLAB script was used to communicate with the Arduino board and automatically start, stop and change the operating frequency of the mechanism.

3.2.2.B Step Mechanism

A test bench capable of applying a sudden displacement of known amplitude on an IPMC sample was also created, as a means of acquiring its electrical response to an approximated step input.

A silicone part encapsulating an IPMC sample, which will be presented in section 3.2.3.D was vertically fixed to a rigid support. A solenoid with a rounded tip adapter was placed perpendicular to the silicone encapsulation and centered in the middle of the IPMC strip (figure 3.8). During testing, the solenoid was activated and a fast displacement was applied at the center of the encapsulated IPMC, taking less than 67 ms to complete.

The solenoid activation circuit is shown in figure 3.9

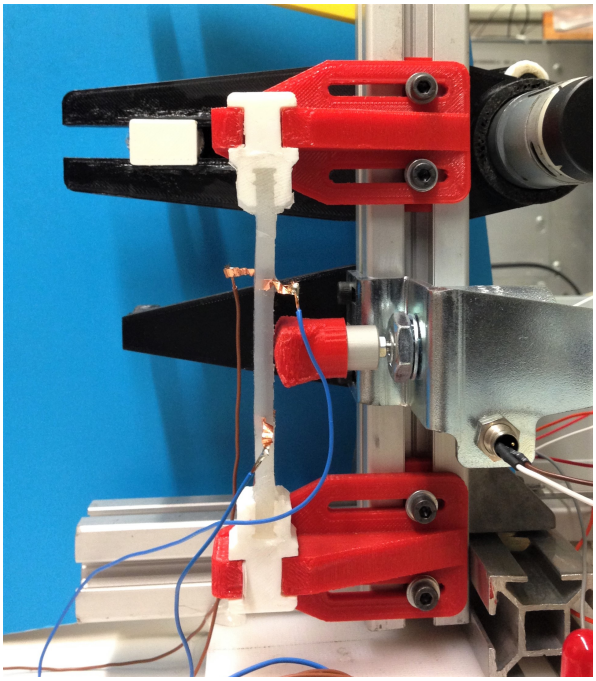

Figure 3.8: Step test bench with aligned IPMC sample, in neutral position.

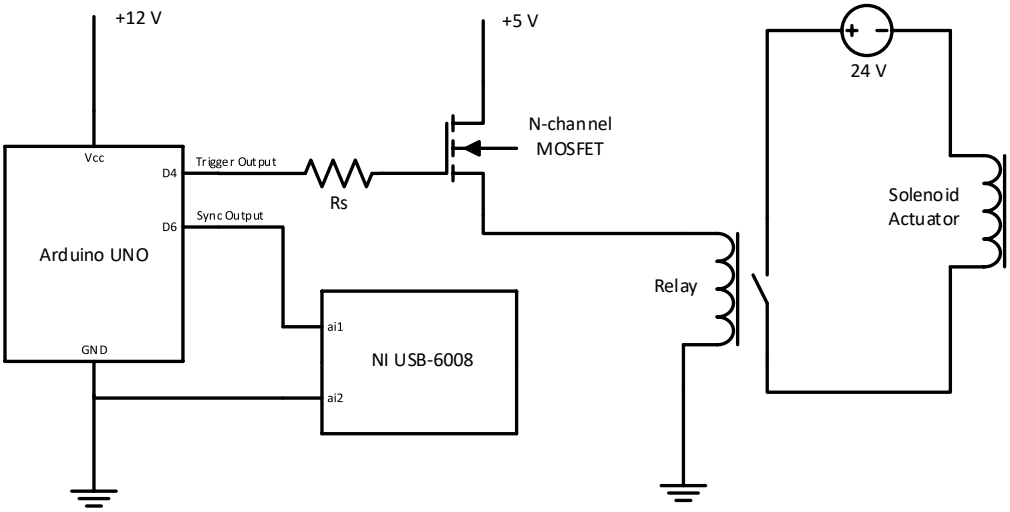

Figure 3.9: Solenoid activation circuit for the step mechanism.

3.2.2.C Signal Amplification and Data Acquisition

During the experiments, a resistor (R_d) was used to connect the two sides (i.e. the two electrodes) of the IPMC. One side was connected to a voltage amplifier and the other to ground potential.

An amplifier circuit made of 3 Op Amp devices was used, in order to amplify the voltage signal obtained from the IPMC circuit to adequate values for the available data acquisition device. The circuit consisted of a buffer and two non-inverting voltage amplifiers, providing a theoretical gain $K_{amp} = 1156$.

For acquiring the voltage signal acquisition from the amplifier to a computer, a National Instruments USB-6008 DAQ was used, interfacing with MATLAB. Each experiment included various consecutive tests at previously specified oscillation frequencies, which were initiated and stopped automatically, following a MATLAB script.

The amplification circuit described is represented in figure 3.10.

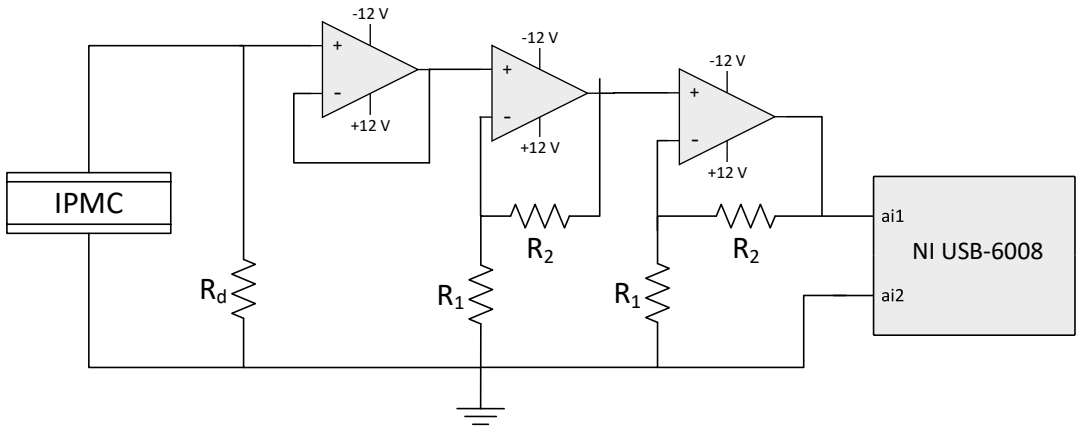

Figure 3.10: Signal acquisition and conditioning circuit. R_1 and R_2 are 1 kΩ and 33 kΩ resistors, respectively, with R_d changing according to the tests performed. Inputs $ai1$ and $ai2$ of the acquisition board were used in differential mode.

In order to amplify the IPMC output from values in the lower mV range to values between -5 and 5 V, two amplification stages were used. These were implemented as non-inverting amplifier circuits, using 741-type Operational Amplifiers. Because of the high gain of the two amplifier stages combined, any small DC offset in the buffer outputs due to input bias currents would be amplified by the following stages, causing a large deviation in the amplifier output. Although with less influence on the final signal, the same also occurred with the two non-inverting amplifier stages. This phenomenon required the use of the *Offset Null* pins in the 741 operational amplifiers to reduce the final offset, as shown in figure 3.11.

On each amplifier stage, a 10 $k\Omega$ potentiometer was connected to each *Offset Null* pin, to allow for manual adjustment of the offset, and a 1 $k\Omega$ resistor was used to connect these to the -12V supply, to avoid the possibility of short-circuit in case one of the potentiometers was improperly adjusted.

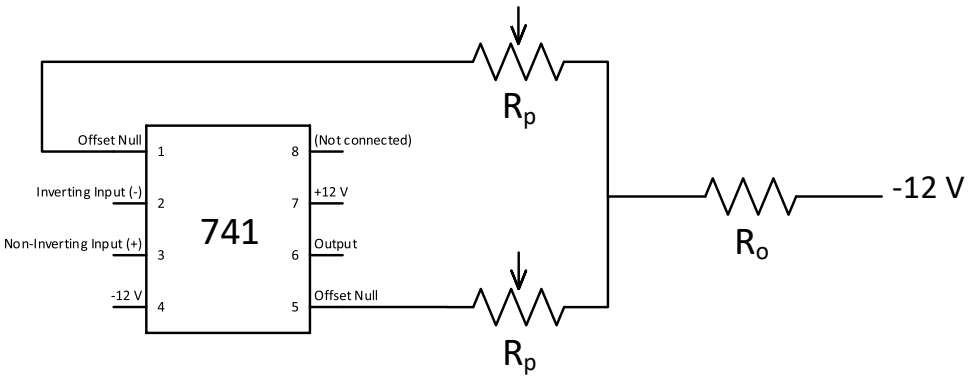

Figure 3.11: Operational amplifier offset compensation circuit. R_p represents a 10 kΩ potentiometer and R_o a 10 kΩ resistor.

On each test, the data was acquired at a sampling frequency of 500 Hz during 20 seconds. Before each acquisition started, the oscillator would run at the test frequency during 5 seconds. This was done to help dissipate any transient effects that could occur in the beginning of the actuation.

After signal acquisition, a Fourier transform was applied to every IPMC response obtained in the same test. The dominant frequency of each test was detected and its amplitude was saved. The amplitudes of the first 2 harmonics were also added to the dominant frequency amplitude, to account for the imperfect sinusoidal nature of the oscillations.

For each experiment, a frequency response graph was created, after obtaining the amplitudes for each test frequency.

3.2.3 IPMC Samples

Three samples of IPMC were cut from a larger piece, manufactured by Environmental Robots, Inc., and used during the tests. Sample 1 was kept without electrolyte, Sample 2 was inserted successively in electrolytes with 5, 15, 25 and 35 g/l as the tests progressed and Sample 3 was tested only with the 15 g/l electrolyte, for validation purposes.

3.2.3.A Dimensions

The main dimensions of the three IPMC samples used, shown in table 3.1, were measured with a caliper, with a precision of $\pm$ 0.05 mm.

Table 3.1: IPMC sample dimensions

Dimensions	Sample 1	Sample 2	Sample 3
Length (mm)	44.5	45	45
Width (mm)	7.5	8	8
Thickness (μm)	200	200	200
Pt Electrode Area (mm2)	333.75	360	360

3.2.3.B Mass

Each of the IPMC samples was weighed with a precision of $\pm$10 mg. The measured values are as described in table 3.2.

Table 3.2: IPMC sample mass

Property	Sample 1	Sample 2	Sample 3
Mass in dry condition (mg)	140	-	160
Mass in wet condition (mg)	-	170	190

Sample 3 was weighed before and after electrolyte absorption. This allowed for an estimation of ingested electrolyte mass to be made, by subtracting the initial mass from that obtained in wet condition. The estimated electrolyte ingestion was 30 mg. In the wet samples, the remaining solution droplets were removed from the surface prior to weighing.

3.2.3.C Electrolyte

For its effect on the IPMC performance as an actuator, described in [34] and [24], an electrolyte with Lithium counter-ions was chosen. The solvent used was Propylene Carbonate, due to its low propensity for evaporation at atmospheric pressure and ambient temperature.

To prepare the solution, *Bis(trifluoromethane) sulfonimide lithium* salt was dissolved in Propylene Carbonate in specific concentrations. The salt and solvent were produced by *Sigma-Aldrich* ®, the former having a purity of at least 99% and the latter at least 99.7%.

Four electrolyte solutions with different lithium salt concentrations were prepared: 5 g/l, 15 g/l, 25 g/l and 35 g/l. These were used in the wet samples for the frequency and step response experiments. Each sample was immersed in the electrolyte for at least 48 hours, before being encapsulated for testing.

3.2.3.D Sensor Encapsulation

The IPMC was encapsulated using *Ecoflex 0030*, a silicone material manufactured by *Smooth-On, Inc*. Two types of encapsulation were used: the first (type 1) was a slotted silicone part on which the IPMC was inserted in after the curing process; the second (type 2) was similar to the first part, but the silicone was cured with the IPMC and contacts directly embedded. The first type of encapsulation allowed for sliding to occur between the IPMC and encapsulation walls, as these were bent by the oscillating mechanism. On the other side, the silicone in the type 2 encapsulation adhered directly to the external surface of the contacts and the IPMC electrodes, and did not allow for sliding movement between these parts.

While the type 2 encapsulation effectively closed the IPMC from the outside environment during the curing process, the type 1 version had an open slot, which was closed with silicone before tests with electrolyte. This helped contain the liquid solution around and inside the tested sample.

3.2.4 Experimental Procedure

3.2.4.A Frequency Response Tests

Harmonic oscillation tests were performed with various IPMC samples using different electrolyte concentrations. For this purpose, the crank-based mechanism described in section 3.2.2.A imposed an approximately-sinusoidal displacement to the center of the encapsulated IPMC, while oscillating at the required frequencies.

Two different encapsulation methods were used, designated as *type 1* and *type 2*, described in subsection 3.2.3.D. The IPMC samples were tested in five different configurations: electrolytes with 5, 15, 25 and 35 g/l of solute concentrations, and no electrolyte.

Before starting the experiments, the encapsulated sensor module was inserted in the test stand and a test measurement was made. When required, the voltage signal entering the amplifier was checked to be within acceptable bounds, in order to avoid saturation. After the amplifier offset was adjusted, a signal acquisition was performed with the IPMC in neutral position, to allow for the characterization of the output noise.

The testing process was controlled by a purposely developed computer algorithm, which started, stopped and changed the rotational frequency of the motor, while also saving the acquired data.

3.2.4.B Step Response Tests

So as to complete the information acquired with the frequency response tests, additional step response experiments were devised.

The testing equipment was composed of the same signal conditioning and acquisition devices used in the frequency-response tests (two-stage amplification with buffer and NI-USB 6008 DAQ), but instead of the oscillating crank mechanism, a solenoid was used to rapidly induce a deformation in the encapsulated IPMC sensor.

The voltage between the two electrodes of the IPMC was measured, while a quick mechanical displacement was imposed, effectively bending the sensor to a predetermined curvature. Because the displacement of the solenoid mechanism is orders of magnitude faster than the normal actuation speeds of the pneumatic actuator where the sensor should be introduced, this procedure was treated as a step response test.

During the tests, the measurement acquisition was started several seconds before the step was applied, in order to have sufficient data on the initial conditions for a low-pass filter to be applied. The measured signal was sampled at 500 Hz, and a synchronization signal was sent from the microcontroller board to the acquisition device immediately after activating the solenoid. With the added load of the sensor and silicone encapsulation, the solenoid response time was found to be less than 66.7 milliseconds.

Each step had the necessary duration to capture the IPMC response at least until its amplitude decayed to less than 5% of the maximum amplitude. After the solenoid retracted, the next step would only be applied after 1.5 times the time of the previous step, so as to allow the signal to be stationary.

The IPMC strip was held in place by the same silicone encapsulation (type 2) described in subsection , and the sensor was placed vertically in front of the solenoid mechanism. On each step, the actuation mechanism induced a displacement of 9 mm on the center part of the sensor. Because the sensor was approximately 1/3 of the total length of its encapsulation, the relative displacement between the center and tips of the IPMC was lower than the aforementioned value.

The empirical displacement measurements allow for the estimation of the sensor curvature in its deformed state.

Preliminary step response tests were performed without having both electrodes of the IPMC connected to a resistor. This way, one of the electrodes was connected to the buffer input of the amplifier (high impedance) and the other to the ground. The results of these measurements were found to be highly variable: after a step was applied, the voltage between the electrodes would slowly drift upwards and downwards, and no pattern was identified. In order to correct this problem, while maximizing the time constant of the signal decay, tests with various resistance values were made and a suitable resistor was selected for the final configuration, based on the results.

3.2.5 IPMC Stiffness Estimation

According to [35], the stiffness of the Nafion membrane changes significantly with the level of hydration. This, coupled to the fact that the mean platinum layer thickness is difficult to estimate and can vary between samples, made the theoretical calculation of the IPMC Young's Modulus impractical. To overcome this problem, it was concluded that this parameter had to be determined experimentally through non-destructive tests. For that purpose, a free vibration analysis of the IPMC sample 2 was performed, using its output voltage signal, measured with the circuit described in section 3.2.2.C.

For performing the test, the IPMC was clamped in a horizontal position between two contacts, with the platinum layers facing sideways (figure 3.12), and a short mechanical stimulus was applied to the tip.

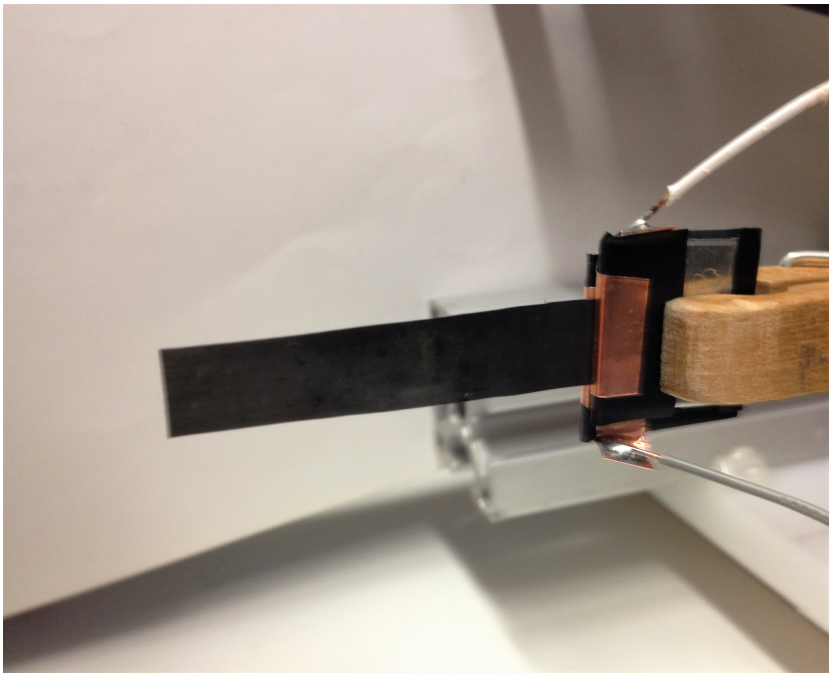

Figure 3.12: IPMC sample 2 clamped for vibration testing.

From the tests performed, a Young's Modulus of $E = 1011$ MPa was estimated. This value stands between the estimates given by [35] and [29], and will be used in section 2.2.5 for defining the material properties in a finite element analysis.

3.2.6 Model Fitting

Based on the results obtained from the frequency and step response tests for the best sensor configuration, a model can be fitted to describe the electrical behavior of the IPMC when a deformation is imposed.

Given the limitations of the available equipment regarding its frequency range and the results that will be discussed in section 4.1.3, it was decided that the frequency test results would not be used directly for model estimation purposes. Instead, the time response data obtained from the step tests was used to estimate the parameters of a transfer function model.

The model identification was done using specialized software. Firstly, a mean of six step responses in the chosen sensor configuration was calculated, and the result was filtered with a low-pass FIR filter, which will be further detailed in section 4.1.6. Secondly, the response data was normalized by the measured sensor curvature caused by the displacement of the solenoid mechanism, which will be presented in section 4.1.1. Finally, a transfer function model with the desired structure was estimated using a model fitting tool. An identification algorithm estimated the parameters for the transfer function, given a "zero" initial condition, the measured system response and input data. Because the response values were normalized, a perfect unit step was used as the system input for estimation.

3.3 Benchmark Actuator

In this section, a benchmark soft pneumatic actuator, used for validation purposes, is described, along with the manufacturing methods used.

A prototype was built with the aim of validating the manufacturing techniques and materials for the final actuator, as well as the finite element model that was developed. Additionally, this prototype will serve as a benchmark for comparing the performance of the final prototype, which will include IPMC sensors.

3.3.1 Molds

Pneu-net actuators manufactured using the standard method, described in [6] may easily present unwanted deformations during use, due to chamber wall thickness irregularities. One possible cause for these defects is the fact that after pouring the silicone in the mold, its free surface is uneven, and usually concave. This allows the thickness of the upper chambers to vary along the length and width of the actuator, and may also yield inconsistent results if multiple equal parts are to be produced. Also, the lower part of the actuator, which includes the inextensible layer, may suffer from similar problems, since the nearly-inextensible material is not precisely positioned along the thickness and its upper surface may also be uneven.

To solve these problems, a modified manufacturing method was used, which allowed for better dimensional control, at the expense of introducing an additional mold-preparation step and requiring slightly more complex mold parts.

A standard mold is comprised of two parts - one for the main chamber body (with the air chambers) and another for the lower layer. On the other hand, the new modified mold has a total of five parts, which fit together to cast the two parts of the actuator.

The modified main body mold, shown in figure 3.13, has been designed to be in a horizontal position while the silicone is poured, to allow it to cover all the chamber negatives without trapping air bubbles. Then, a cap is introduced to the top of the mold and fixed with rubber bands, so that the mold can be rotated to stand vertically. When in vertical position, another cap can be removed to expose the free surface of the silicone in the upper part of the mold and allow any additional air bubbles to be released. By letting the silicone cure with the mold in a vertical position, the free surface of the liquid will be on a non-critical face of the main body. That region is later connected to the actuator support, where more silicone can be added to cover irregularities. In case air bubbles are still trapped in the silicone after curing, this will also be the most likely place for them to be. By moving the least-controlled geometry to a non-crucial zone of the actuator, this method allows its most sensitive dimensions to be kept within tighter tolerances during the curing process.

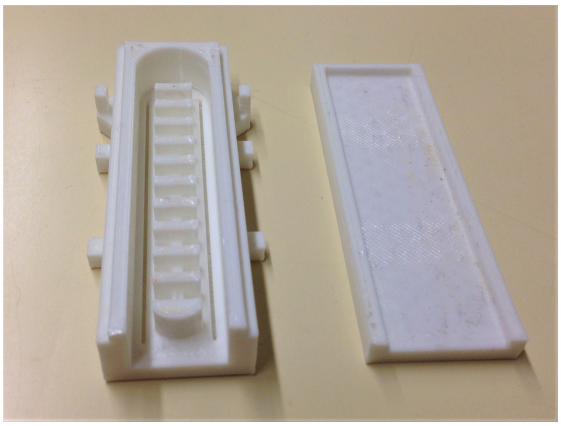

(a) Main body mold parts, open configuration.

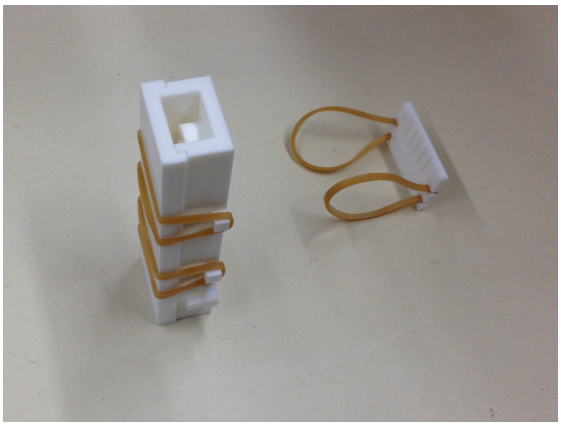

(b) Lower layer mold parts, closed.

Figure 3.13: Main body mold, in open and closed configuration.

The lower layer mold (figure 3.14) was composed of two parts that are attached to each other during the curing process. The nearly-inextensible fabric is inserted between the two parts, so that it remains stretched when these are joined. This ensures its correct positioning during the whole procedure. Since this mold has no complicated geometry that might retain air bubbles, it is directly filled with silicone in a vertical configuration.

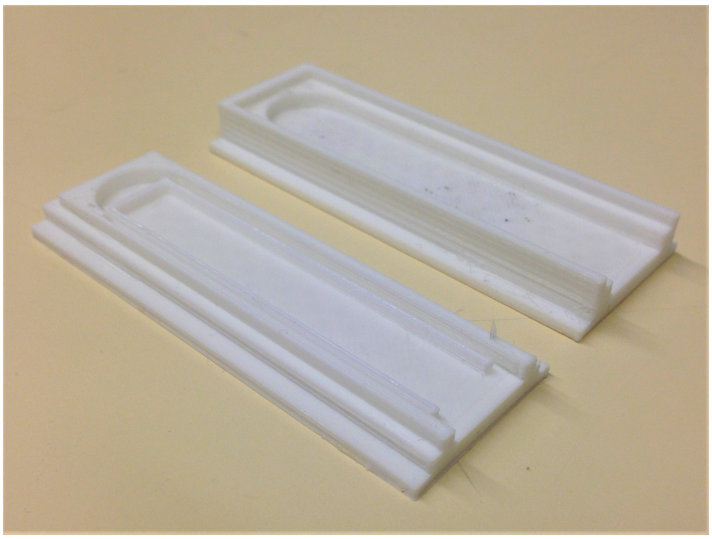

(a) Lower layer mold parts, open configuration.

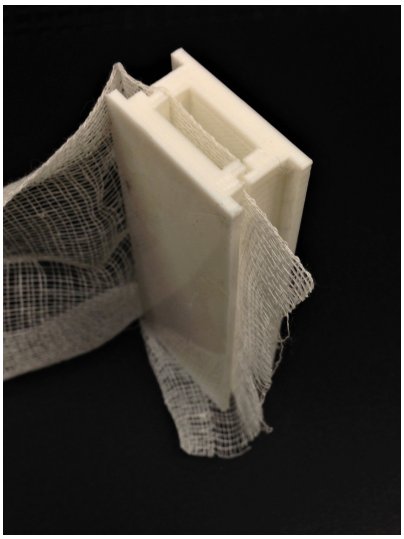

(b) Lower layer mold parts, closed with nearly-inextensible fabric.

Figure 3.14: Lower layer mold, in open and closed configuration.

To aid in the alignment of the main body with the lower layer of the actuator when joining those parts, the molds were designed so that both fit together: the former has a protrusion in the face that will be bonded, while the latter has a groove. This also increases the surface area between the two parts, providing greater bonding strength.

The mold parts were manufactured in PLA, using a 3D printer with a layer resolution of 200

μm.After printing, small surface imperfections (grooves) were detected in the molds. Those existent in the critical parts of the molds, such as the air chamber negatives, were covered with acrylic lacquer.

3.3.2 Manufacturing Process

The manufacturing process of this Pneu-net actuator is based largely on casting pre-mixed Ecoflex® 00-30 silicone into specially designed molds, and joining the cured parts using the same liquid silicone.

The actuator body was manufactured in four main steps:

- Two separate parts were produced, comprising the base of the actuator with the inextensible layer and the chamber body.
- After the chamber body finished curing, a hole was cut at the base and the tip of a rubber air tube was inserted and bonded with silicone.
- The upper and lower parts of the actuator were aligned and joined with silicone.

Before starting the pouring process, the joints between the fitting parts of the molds were covered with a thin layer of silicone, and slightly cured to a point at which they were still slightly viscous. This allowed for a good seal when the mold parts were fitted together.

After preparing the molds, the silicone was poured (figure 3.15) and cured at ambient temperature, following the procedure described in section 3.3.1. After curing for at least 4 hours, the silicone parts were removed from their respective molds (figure 3.16) and the excess material was cut.

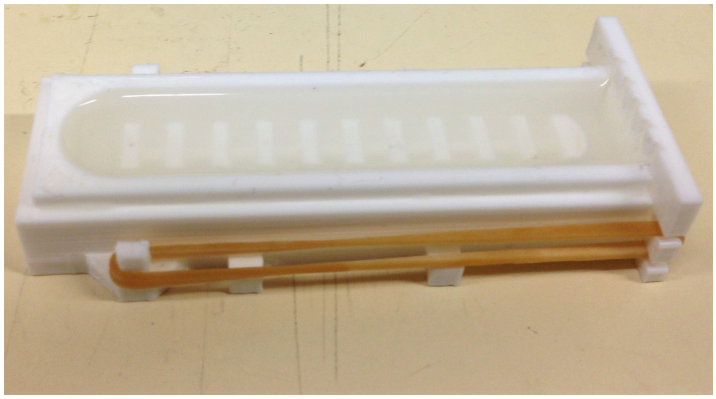

Figure 3.15: Main body mold filled with silicone.

(a) Lower silicone part after curing.

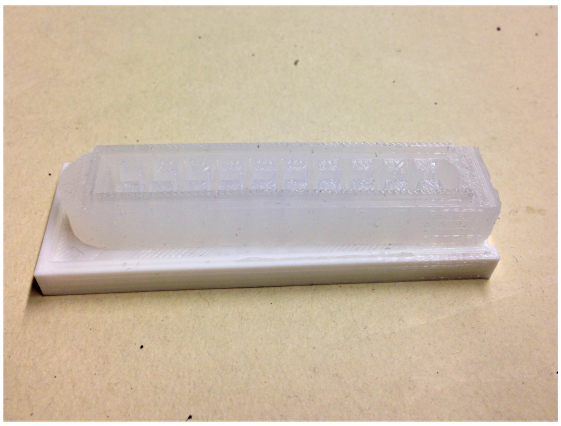

(b) Main body silicone part.

Figure 3.16: Lower and main body silicone parts, after curing.

When joining the upper and lower parts, a uniform pressure was applied to push them against each other and avoid the formation of air bubbles in the liquid silicone interface.

The base of the actuator was bonded to a 3D-printed encasement (figure 3.17) with corrugated internal walls. This rigid part allowed for the actuator to be mounted on a test stand.

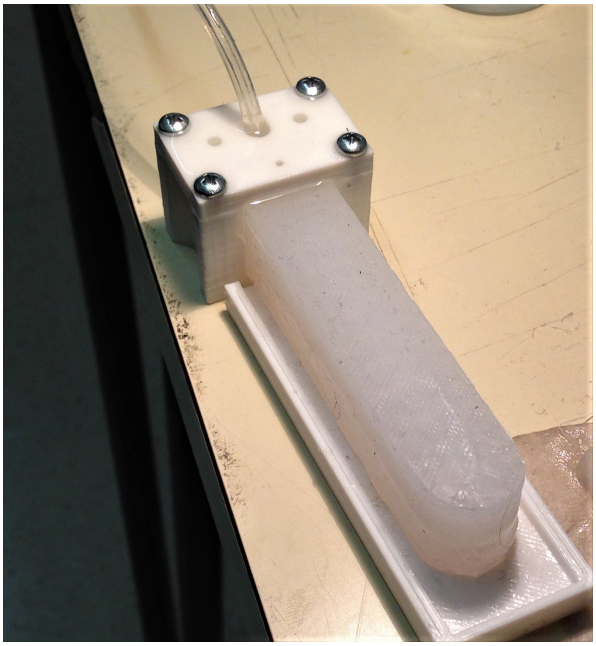

Figure 3.17: Benchmark prototype with plastic encasement at the base.

3.3.3 Test Bench

To simplify the actuator displacement measurements, a test stand was conceived, with a vertical support frame and a measurement scale. The actuator was mounted to the frame in a horizontal position, so that the silicone body only be supported by the plastic encasing. An acetate sheet printed with a millimeter scale was fixed to the vertical frame, as close to the silicone body as possible, to allow for visual measurements of the actuator deformation. The assembled test bench is shown in

figure 3.18.

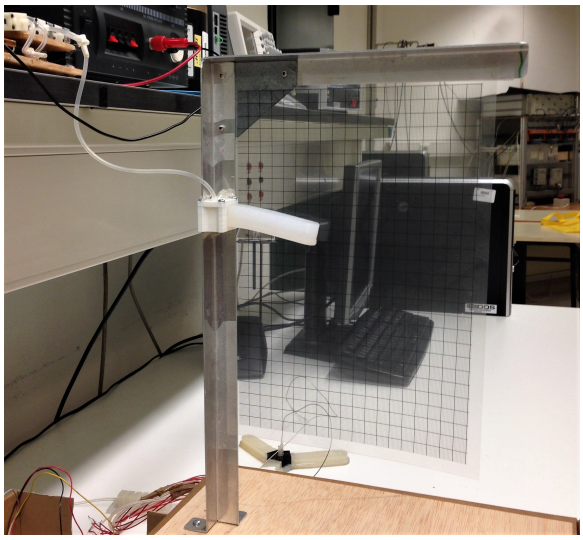

(a) Back view.

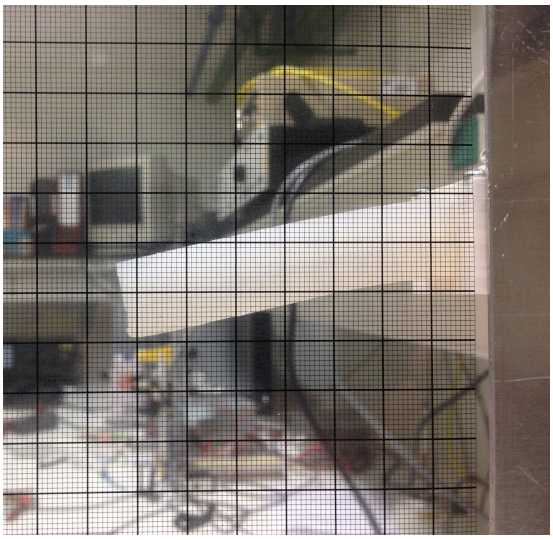

(b) Front view - region of interest.

Figure 3.18: Benchmark actuator mounted on the test bench.

For testing the benchmark prototype, the air tube of the actuator was connected to a pump, a solenoid valve and a pressure sensor.

3.4 Instrumented Pneu-net Prototype

Using an IPMC sensor in the best configuration tested (as will be presented in section 4.1.2) and the geometry from the benchmark actuator, an instrumented Pneu-net actuator was developed.

3.4.1 Description

One of the objectives of using a flexible sensor was to detect the actuator curvature while having a low impact on its stiffness. It was found that an adequate region for its placement would be on the neutral surface of the bending body. Would the actuator hypothetically be subjected to pure bending, that would be the surface where an infinitely thin IPMC strip would neither be under traction nor compression. In practice, this would mean placing the sensor directly in the inextensible layer. That way, only the flexural rigidity of the sensor would affect the mechanical behavior of the actuator.

Since it was not desirable to have an IPMC strip acting as the entire inextensible layer, due to the loads involved, it was chosen to place it directly under this region. As with the benchmark actuator, a coarse cotton fabric was used for that layer. Since this fabric could potentially absorb electrolyte that could escape from the inside of the IPMC, it was decided that a thin layer of silicone should exist between them to prevent that from happening.

Using a similar process to the one used for the *type 2* encapsulation described in section 3.1.3, a *sensing module* was devised, with an encapsulated IPMC strip. This module should integrate with base silicone layer of the actuator and the sensor should be as close as possible to the cotton fabric.

For simplification, the instrumented actuator geometry was the same as the benchmark prototype. Therefore, the main chamber body and base layer were manufactured using the same molds as the latter. Nevertheless, an additional step was required in the manufacturing process, for encapsulating the sensor prior to its insertion in the base layer.

3.4.2 Manufacturing

For manufacturing the *sensing module*, a new mold was created, which made use of cylindrical protrusions to compress the IPMC between flexible copper contacts as the silicone cured, as well as other alignment features, also present in the *type 2* encapsulation method. The mold, shown in figure 3.19, was composed of two parts, which were pressed together during the curing process, using rubber bands.

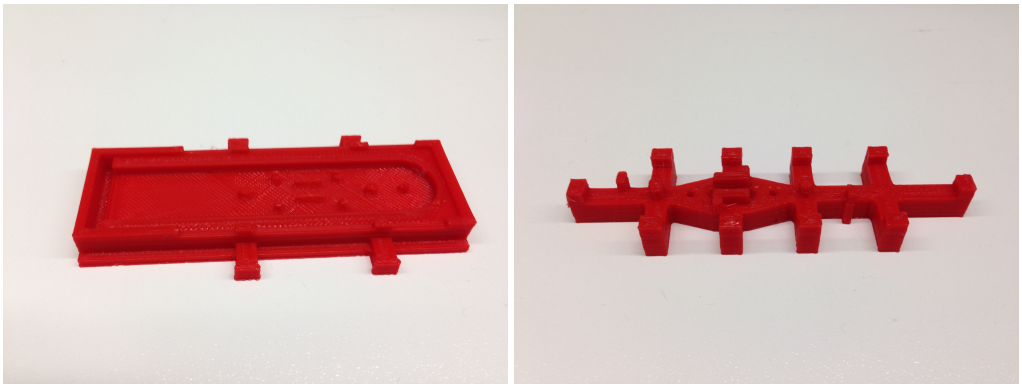

(a) Lower part. **(b)** Upper part.

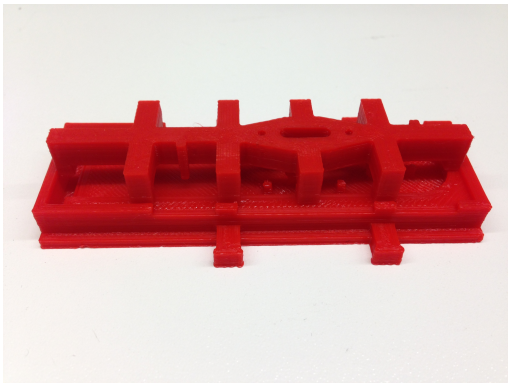

(c) Assembled.

Figure 3.19: Sensing module mold.

The copper contacts were cut from a copper adhesive tape. After a thin layer of silicone was cured over the protrusions where the IPMC and contacts would stand on, the latter were fitted to the mold (figure 3.20-a). After that, the IPMC was aligned over the contacts (figure 3.20-b), the mold was closed and liquid silicone was poured through the openings of the upper mold part.

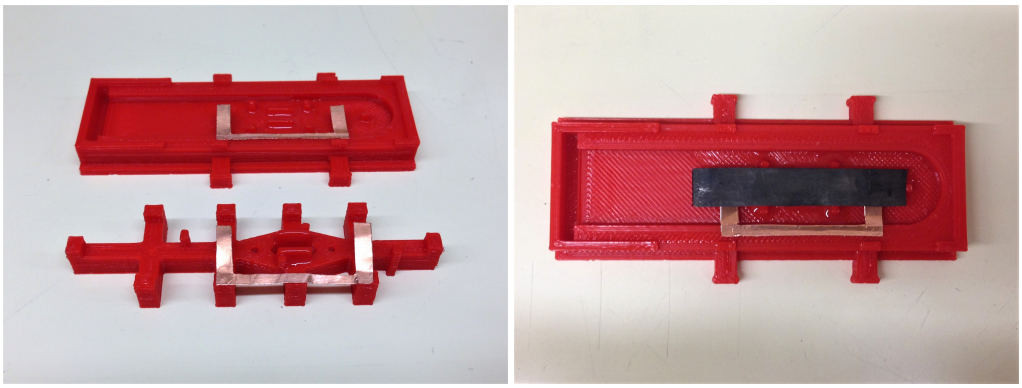

(a) Flexible copper contacts fitted. **(b)** IPMC and lower contacts aligned.

Figure 3.20: Contact alignment and IPMC placement inside the mold.

The resulting silicone part, after curing, is shown in figure 3.21. As can be observed, there were localized areas where excess silicone was accumulated. These irregularities had to be removed before proceeding to the next manufacturing step.

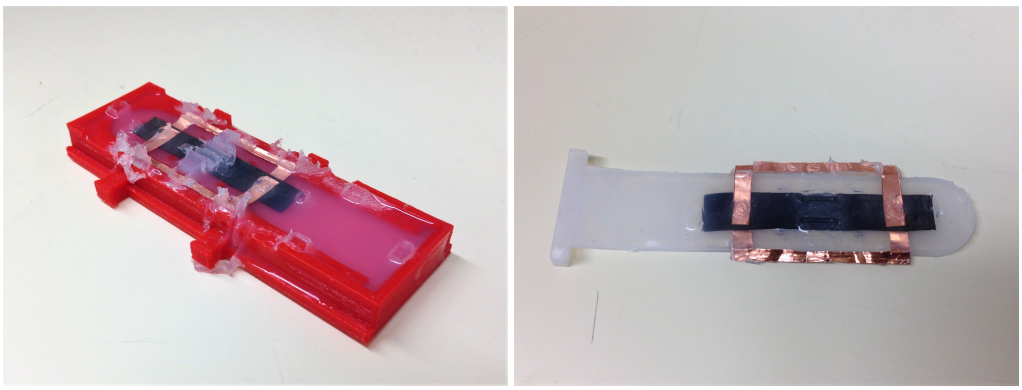

(a) Sensing module after curing. **(b)** Sensing module after removing excess material.

Figure 3.21: Sensing module.

After the *sensing module* was fabricated, it was fitted inside the base layer mold, as seen in figure 3.22-a. The cotton fabric was then placed on top of it, the mold was closed and placed in a vertical orientation and liquid silicone was injected. The resulting base layer with the sensor included is shown in figure 3.22-b.

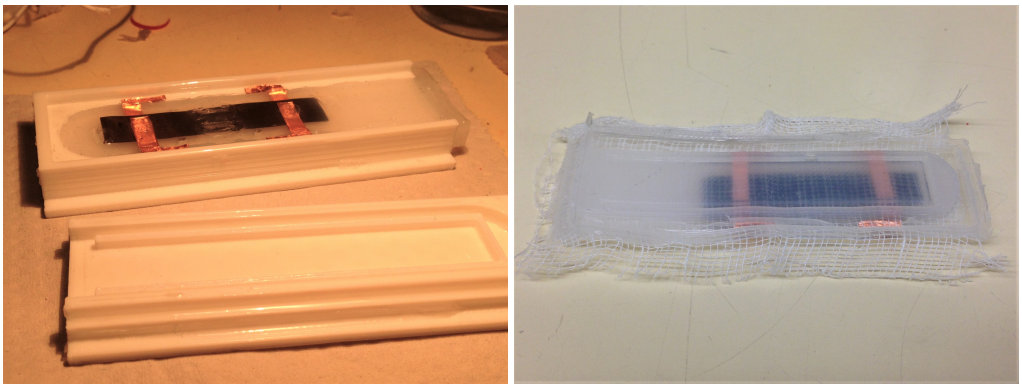

(a) Sensing module fitted in the base layer mold, before sealing and casting.

(b) Base layer after curing.

Figure 3.22: Base layer manufacturing for the sensing actuator prototype.

Similarly to the benchmark actuator, the base layer and main body were joined, and the exposed contacts (figure 3.23) were used for testing the electrical connection to the IPMC surface electrodes.

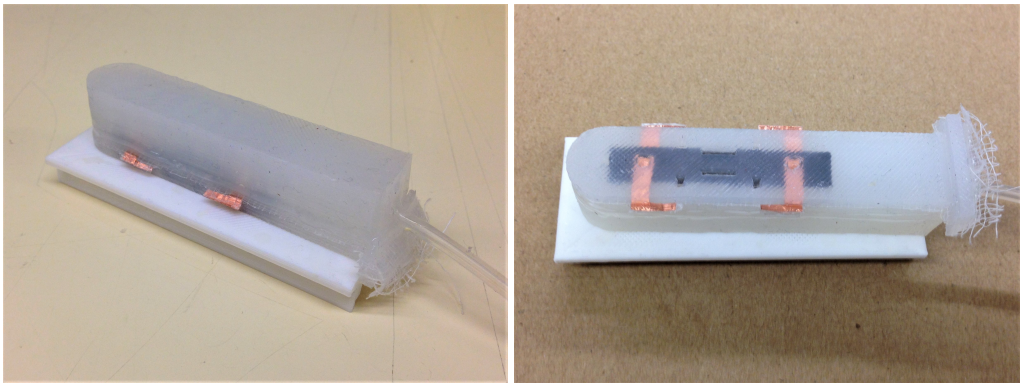

(a) Perspective view.

(b) Bottom view.

Figure 3.23: Instrumented actuator after joining the base and chamber body parts. Exposed contacts used for testing electrical contact.

To finish the actuator, a thin copper wire was soldered to each pair of contacts, connecting those on the same side of the IPMC. The wire was bended in a wave pattern, so that it could stretch slightly in case the actuator bended sideways or upwards, reducing the stress applied in the contacts. A thin silicone layer was then added over the cables and exposed contacts, to insulate them from the external environment.

The final prototype, as seen in figure 3.24, has a plastic encasing at the base, housing two connectors for acquiring the electrical signal coming from the IPMC sensor.

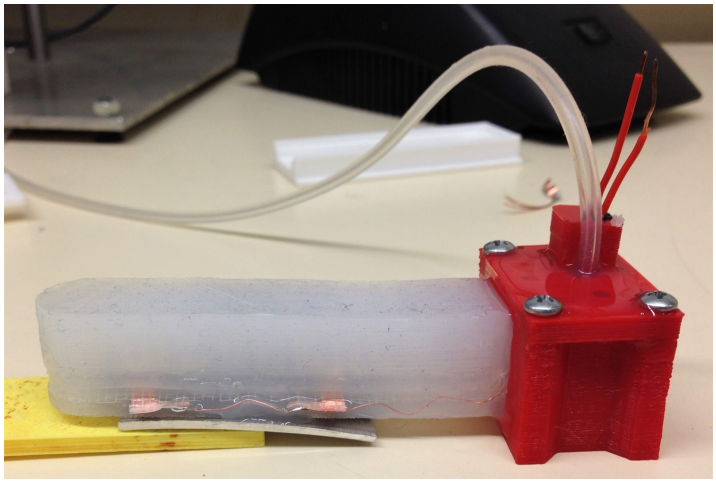

Figure 3.24: Finished instrumented pneu-net.

3.4.3 Curvature Measurements

Using the same technique described in section 4.1.1, the curvature of the actuator was measured for various loading values. For synchronizing the sensor output with the curvature on each instant measured, the instrumented actuator was filmed with an overlaid millimeter scale during the tests, and a LED was turned on when the actuation started, for synchronization purposes. The radius measured is exemplified in figure 3.25

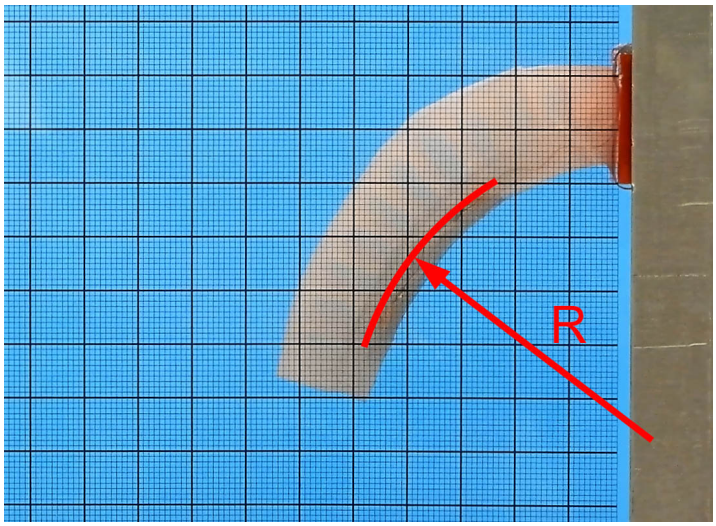

Figure 3.25: Example of the curvature radius of the instrumented pneu-net prototype.

3.4.4 Feedback Testing Procedure

In order to validate the performance of the IPMC sensor in the instrumented pneu-net prototype, tests were performed by inflating and deflating the actuator on the test bench, while acquiring the voltage signal coming from the sensor. The actuator was placed behind the semitransparent millimeter scale shown in section 3.3.3, and a camera was used to record a video of the actuation. The curvature of the actuator length covered by the IPMC was evaluated on several frames corresponding to critical points during the inflation-deflation cycle, such as when the inflation/deflation started or ended.

The video and data acquisition were synchronized by means of a light visible during the recording, controlled by the same microcontroller responsible for the actuation, whose circuit was connected to an input on the signal acquisition device. When treating the data, the frame when the light turned on was synchronized with the input sample of the acquired signal on which a falling edge was detected.

The video was captured at 30 fps, while the voltage signal was acquired at 500 Hz. Therefore, the delay between the directly measured curvature and the sensor values should be lower than 34 ms.

The actuation cycle was composed of 1.5 seconds of inflation, 10 seconds idle at an inflated state, valve opening for a quick deflation and 10 seconds idle at a deflated state.

4

Results and Discussion

Results from the IPMC characterization tests are presented. From these results, a comparison is made between tests with various electrolyte concentrations. An empirical model is estimated from step test results. A validation study of the finite element model used for the actuator is performed. A sensing actuator prototype is presented and validated.

4.1 Sensor Identification Experiments

The results from the identification experiments performed with the IPMC test samples will be presented in this section. Based on the frequency response test results, a comparison between the obtained signal amplitude with the various electrolytes tested will be made. Also, relevant data for model estimation, from the frequency and step response tests, will be examined.

4.1.1 Curvature Measurements

For comparing the sensor output with the real input values, its curvature was measured with the respective test benches in a maximum-displacement configuration.

For that purpose, three points were measured along one of the encapsulation contours on each test bench. The radius R_i of the circumference passing through those points, exemplified in figure 4.1, was computed and an offset was added or subtracted, depending on the side of the measured contour. This was done to obtain the radius at mid-thickness, where the sensor is located. The curvatures k_i obtained were calculated by $k_i = \frac{1}{R_i}$.

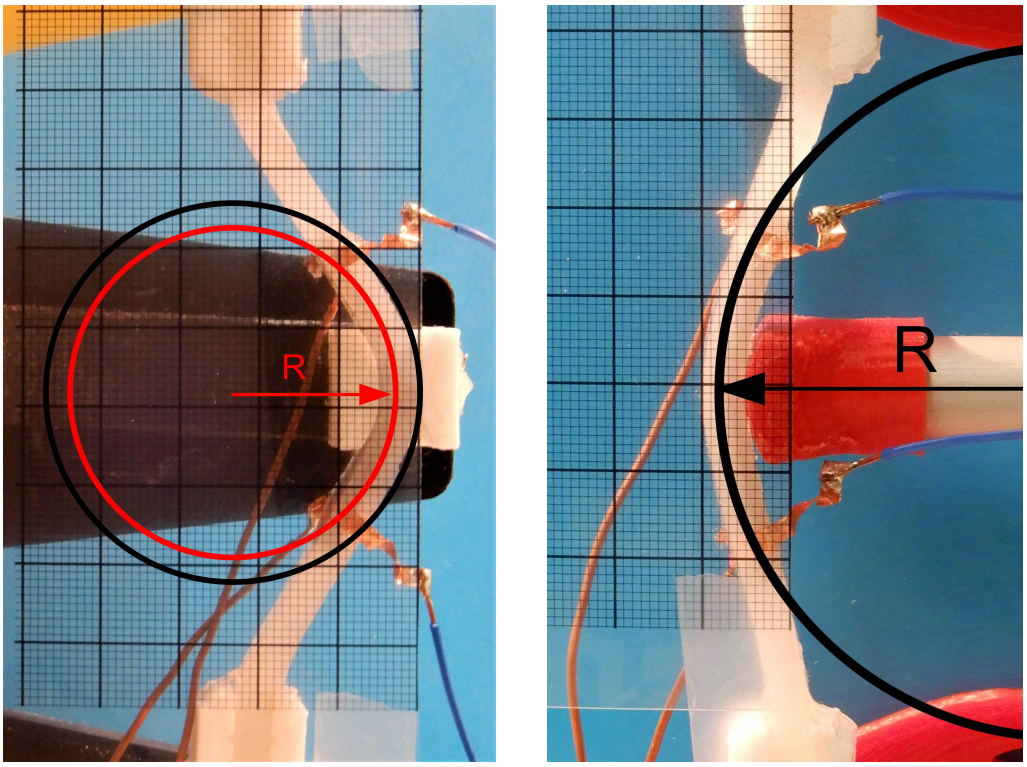

(a) Oscillating test bench.

(b) Step test bench.

Figure 4.1: Approximate radius of curvature in the oscillating and step test benches.

In the frequency test bench, a radius of 37.6 mm was measured, corresponding to a curvature of 0.0266 mm^{-1}. Making the same measurements in the step test bench, the radius was 21.5 mm, resulting in a curvature of 0.0465 mm^{-1}.

4.1.2 Electrolyte Comparison

The oscillation experiments performed with the encapsulated IPMC samples allowed for a comparison between the electrical responses with the various electrolyte concentrations used.

For the electrolyte concentrations of 5 g/L, 15 g/l, 25 g/l and 35 g/l, a second-order polynomial curve was fitted to the valid oscillation test results. These are represented in figures 4.2 and 4.3.

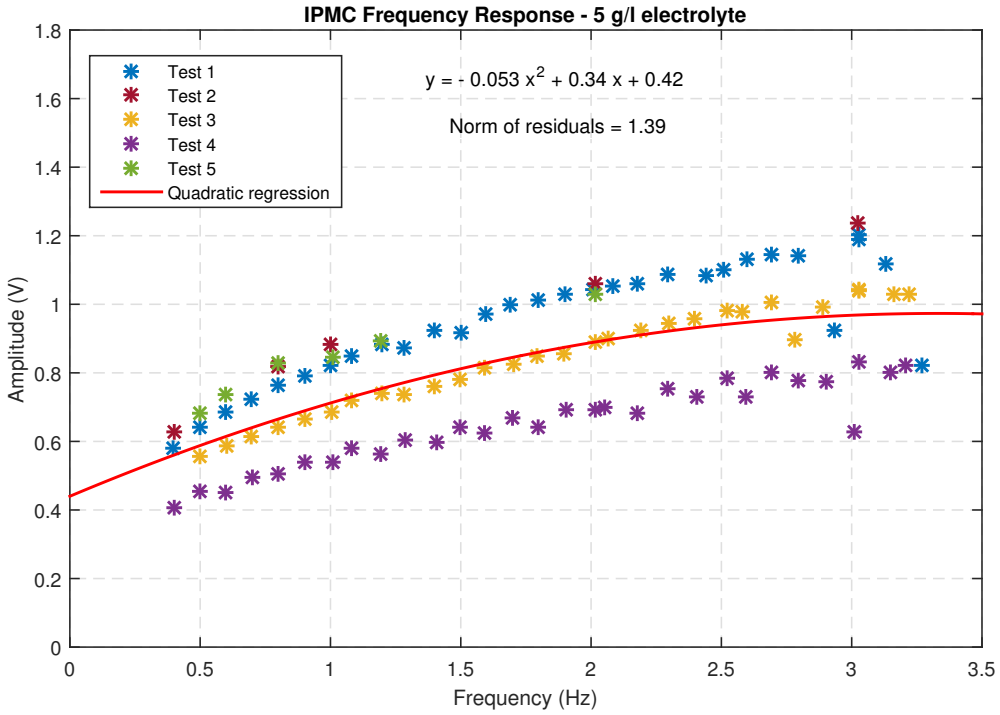

(a) 5 g/l electrolyte.

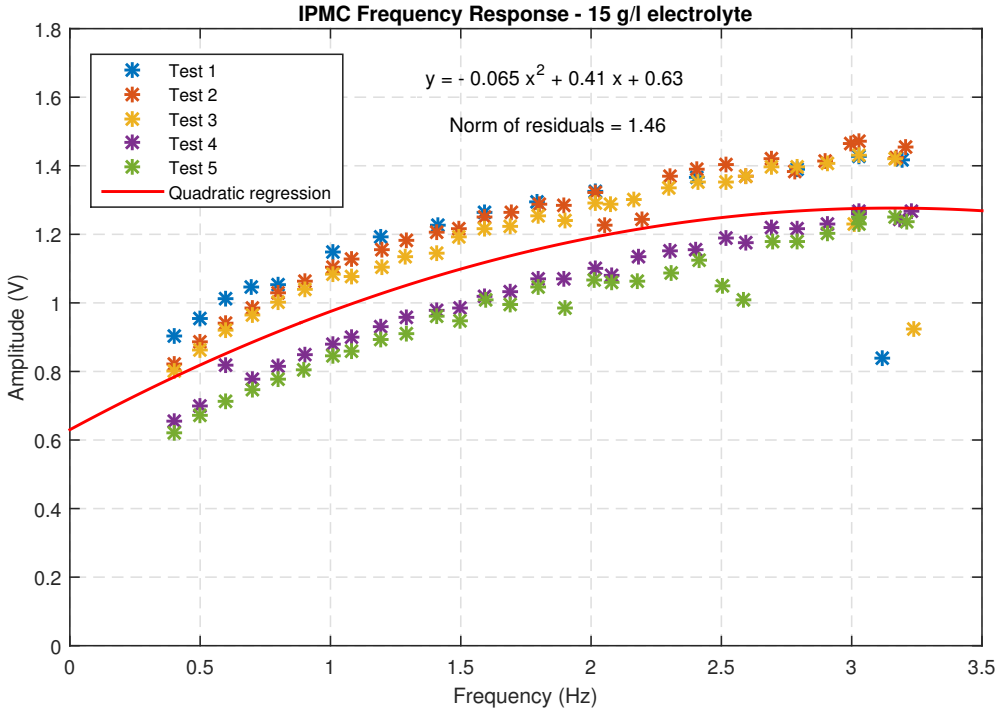

(b) 15 g/l electrolyte.

Figure 4.2: Test results and fitted polynomials for the frequency response of an IPMC sample with 5 g/l and 15 g/l electrolytes.

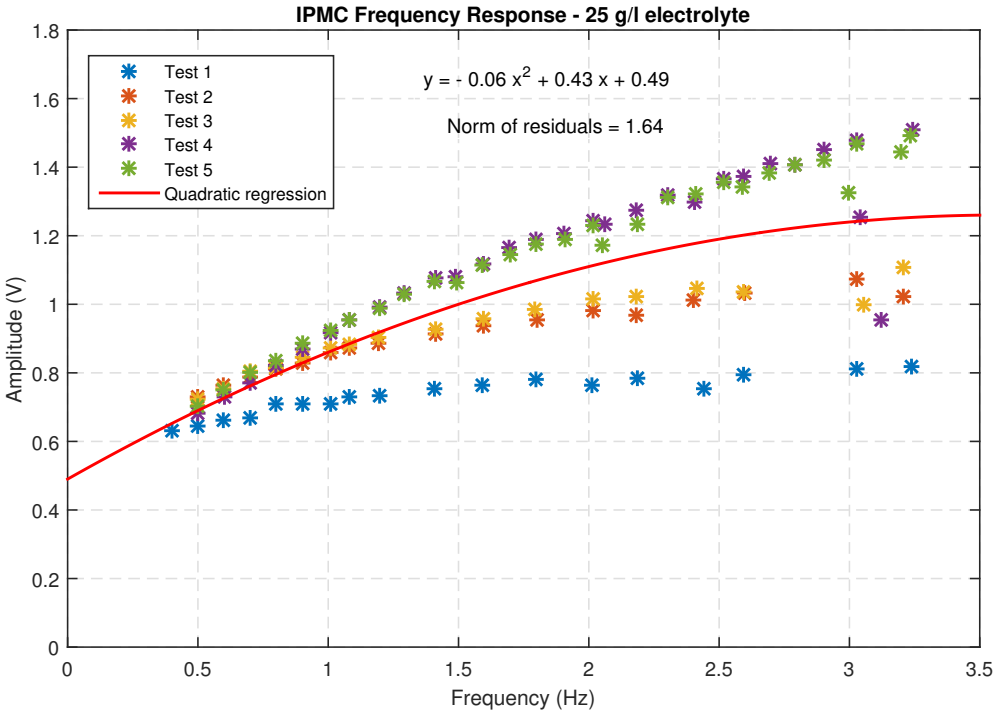

(a) 25 g/l electrolyte.

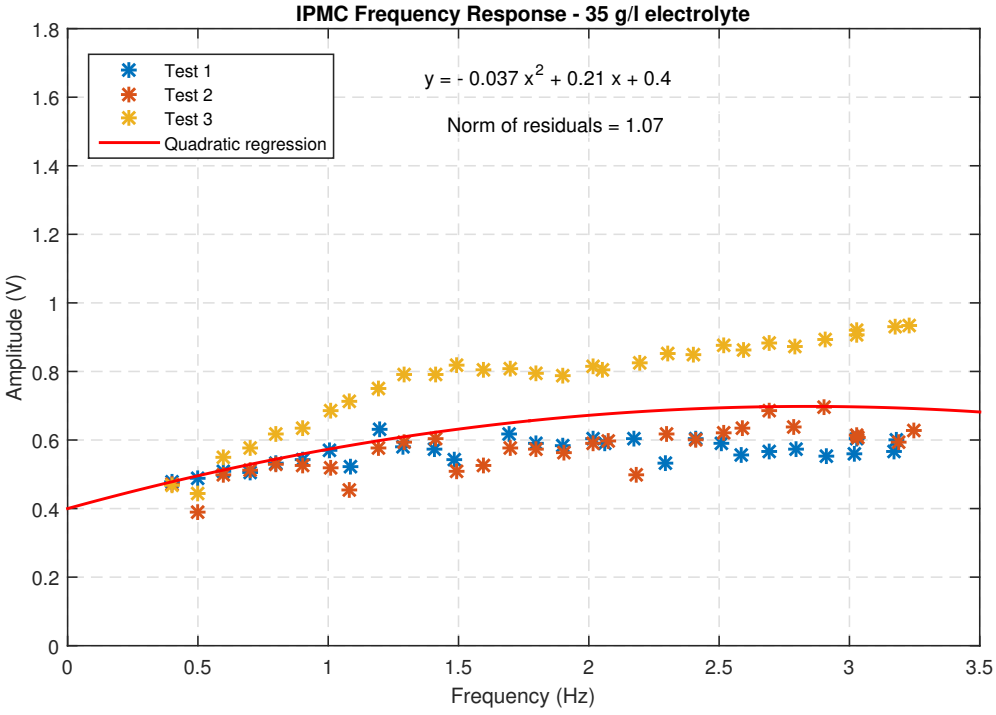

(b) 35 g/l electrolyte.

Figure 4.3: Test results and fitted polynomials for the frequency response of an IPMC sample with 25 g/l and 35 g/l electrolytes.

For comparison, results from the oscillation tests performed without electrolyte are represented in figure 4.4.

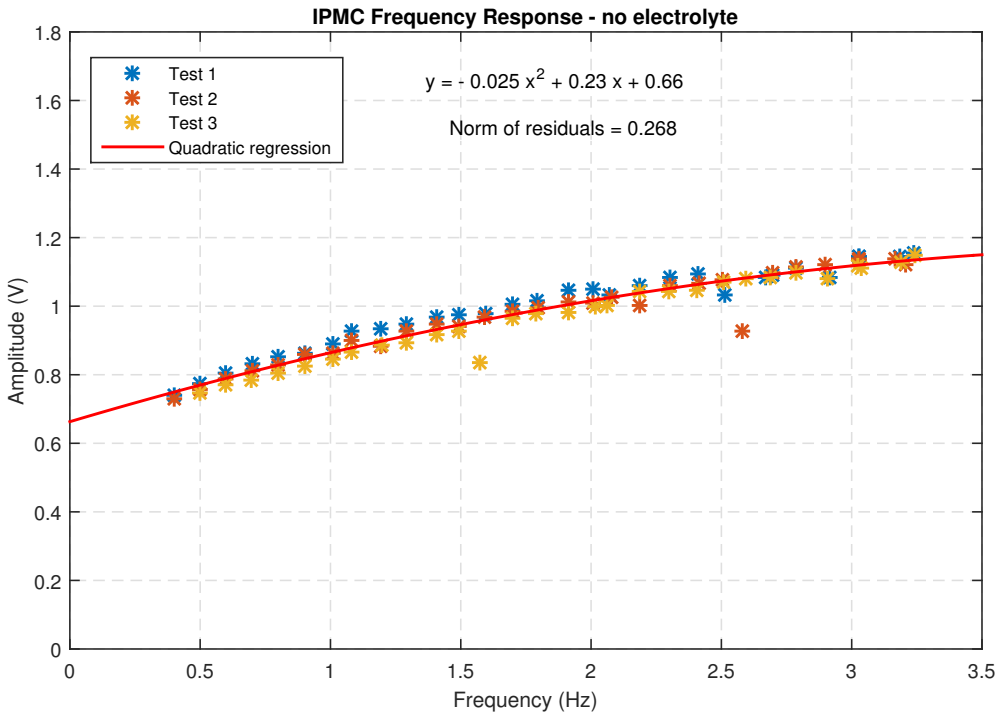

Figure 4.4: Test results and fitted polynomials for the frequency response of an IPMC sample without electrolyte.

As can be observed in figures 4.2 and 4.3, there was a noticeable dispersion in the results, between the various tests performed for each concentration. This dispersion generally increased with frequency. When comparing the results for IPMC samples with and without electrolyte, the latter case had a significantly lower dispersion, with the fitted polynomial achieving a much closer approximation of the experimental results. A possible cause for this may be the redistribution of the electrolyte inside and outside of the IPMC during the applied bending motion, since the type 1 encapsulation used for the previous tests allowed for empty space to exist around the IPMC.

Using the values of the fitted functions at six different frequencies, the results can be represented in a amplitude vs concentration configuration, shown in figure 4.5, which is useful for comparing the performance of the electrolytes. A quadratic curve was fitted to the data points for the highest frequency.

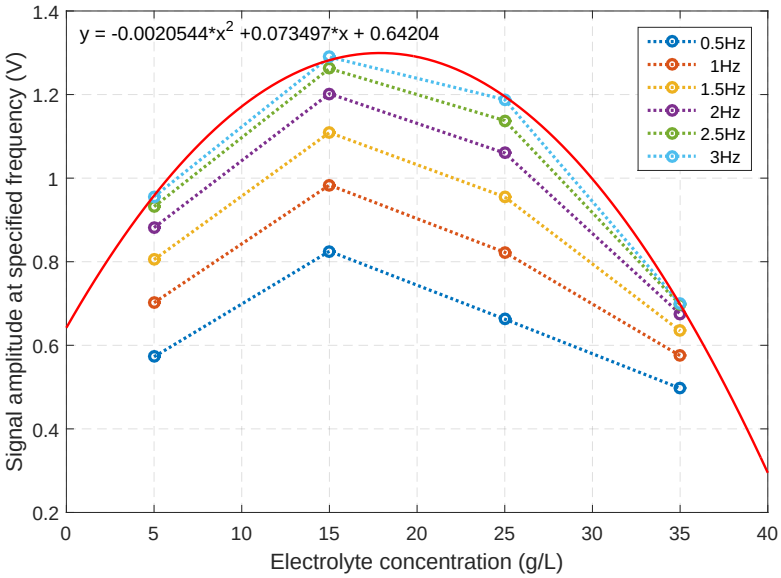

Figure 4.5: Amplitude of the IPMC frequency response versus electrolyte concentration.

From figure 4.5, it can be observed that the amplitude of the IPMC response was highest with the 15 g/l electrolyte. Also, the values for 25 g/l and 35 g/l suggest a descending trend with the increase in concentration. This saturation phenomenon is similar to the one documented in [36], where IPMC samples were being used with a Na^+ electrolyte as energy harvesting devices.

The results with the dry sample show a higher output amplitude than those with the two highest concentrations of Li. The 5 g/l electrolyte also yielded slightly lower amplitude values than the dry configuration.

To assess the effects of the type 2 encapsulation in the oscillation test results, three IPMC samples were encapsulated using that method. Two of the samples were used with 15 g/l and 35 g/l electrolytes respectively, and the third sample was used without electrolyte. The results, presented in A, showed a much lower dispersion than those obtained with the type 1 encapsulation.

4.1.3 Frequency Response

Data from oscillation tests with the 15 g/l electrolyte was compared to that of a sample without electrolyte. Figure 4.6 shows the mean frequency response of the tested samples in those conditions. For calculating the mean, a total of five tests were used in each case.

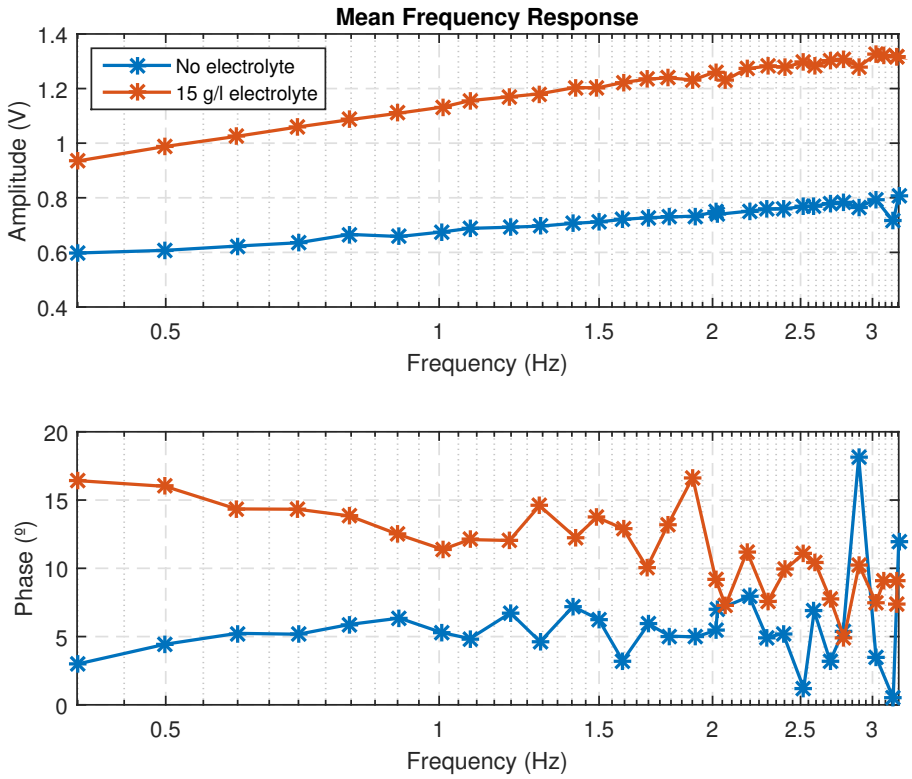

Figure 4.6: Mean frequency response of IPMC samples with a 15 g/l electrolyte and without electrolyte.

Due to imprecisions in the position feedback of the motor connected to the oscillating mechanism, errors of $\pm$ 4º were expected in the phase shift measurements.

The results show a trend of increasing amplitude with the increase of frequency, hinting that a high-pass filter behavior might adequately model the sensor response within the desired bandwidth. This will be discussed further in section 4.1.7.

4.1.4 Performance Evolution over Time

To evaluate changes in the output characteristics of the IPMC sensor during extended operation, a long-duration oscillation test was performed with *sample 3*, spanning several hours.

An electrolyte with 15 g/l concentration was used in the sample, since it produced the highest signal amplitude and lowest variability in the results from previous tests, shown in section 4.1.3. The *type 2* encapsulation was used.

Cyclic deformations at frequencies between 0.75 and 1 Hz were applied to the encapsulated IPMC, during a time span of 7 hours and 10 minutes. In 10-minute intervals, 20 seconds of the IPMC voltage output were acquired and saved. These were later processed using a fast Fourier transform (fft) algorithm and identifying the amplitude at the main frequency, similarly to what was done in section 4.1.3.

The results, presented in figure 4.7 show minor amplitude variations over time, but no decreasing trend seemed to exist. In fact, taking into account the changes observed in the oscillation frequency

and based on the previous frequency response results, the response amplitude of the sensor increased slightly after the first measurements.

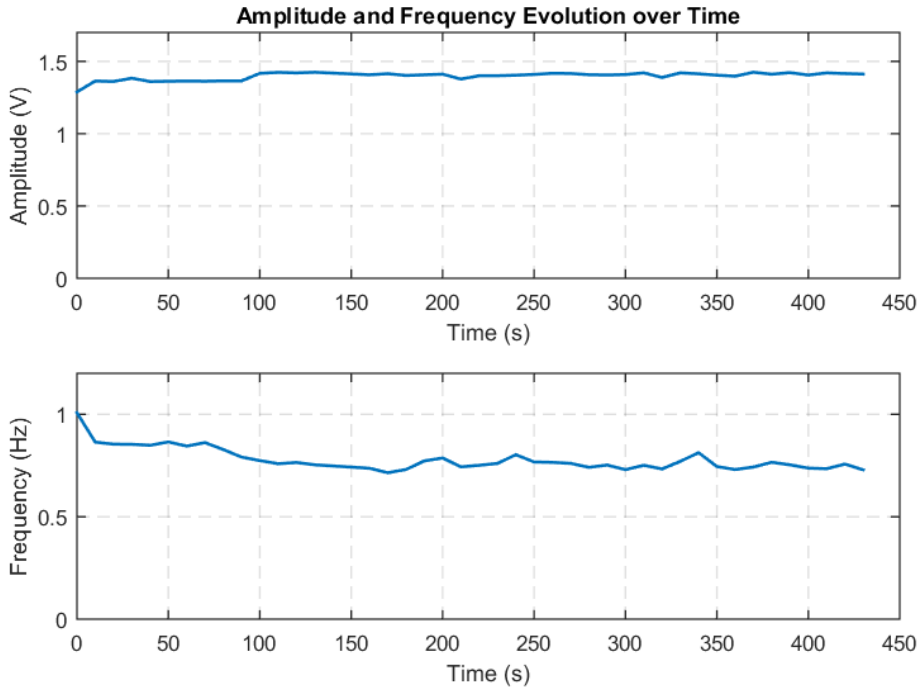

Figure 4.7: IPMC response amplitude during continuous operation.

Due to problems with the motor control system during these tests, as well as possible variations in the power supply, the oscillation frequency varied between 0.7 and 1 Hz.

4.1.5 Noise

To characterize the noise during the experiments, signal samples acquired before the oscillation tests were analyzed with a fast Fourier transform algorithm. The results showed amplitude peaks near 55 Hz and its harmonics, as seen in figure 4.8.

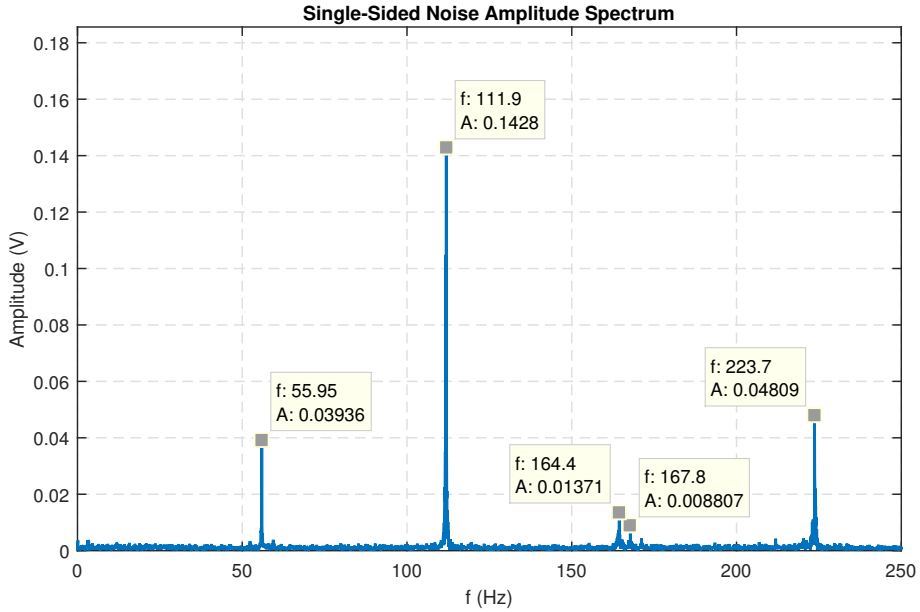

Figure 4.8: Noise amplitude spectrum of the amplified voltage signal, with its main peaks identified. The sensor was maintained in a neutral position, without actuation.

4.1.6 Step Response

Since the frequency spectrum tested was not large enough to capture relevant changes in the amplitude slope and phase shift, it was decided that different tests should be performed to help capture additional information about the system dynamics. For this purpose, mechanical step response tests were performed with the two encapsulated IPMC samples chosen. It should be noted that the mechanically-applied displacement, due to its physical nature, cannot perfectly emulate a step input. Still, it was considered a good enough approximation when using the solenoid actuator mechanism described in section 3.2.2.B.

As with the oscillating tests, the voltage between the two sides of the IPMC was measured with the circuit described in section 3.2.2.C. The experiment was performed with the shunt resistor R_d (previously shown in figure 3.10) taking values between 99.6 Ω and 3.27 MΩ.

For high values of R_d, the tests showed that voltage signal offset drifted considerably during the experiment, and in some cases saturated the amplifier output. For the smallest values of R_d, a notable decrease in signal amplitude and a faster decay was observed. Taking these results into account, a intermediate resistance value of 2.7 kΩ was chosen for the sensor configuration to be further tested and modeled.

In order to remove unwanted noise from the amplified signal, the results obtained from the step response tests and presented in this section were first filtered with a non-causal finite impulse response (FIR) low-pass filter.

Taking into account the noise measurements presented in 4.1.5, a FIR filter was implemented in MATLAB®. This filter type was chosen over the infinite impulse response (IIR) type mainly due to the former introducing a constant delay with the frequency. This allowed for an easy offline removal

of the output delay. For the desired characteristics, shown in table 4.1, the function produced a filter with 407 coefficients, which caused a delay of 203 samples in the output. The normalized frequency values are represented in half-cycles per sample. For the sampling frequency of 500 Hz used for data acquisition, the values of the passband and stopband frequencies were 15 Hz and 20 Hz, respectively.

Table 4.1: FIR filter parameters

Property	Value
Filter Type	Low-pass
Normalized Passband Frequency	0.06
Normalized Stopband Frequency	0.08
Stopband Attenuation (dB)	65
Maximum Passband Ripple Amplitude (dB)	0.5
Design Method	Kaiser Window

After filtering, the output delay was removed from the time response by shifting the results 203 samples forward. A treated step response output can be seen in figure 4.10, superimposed on the original signal.

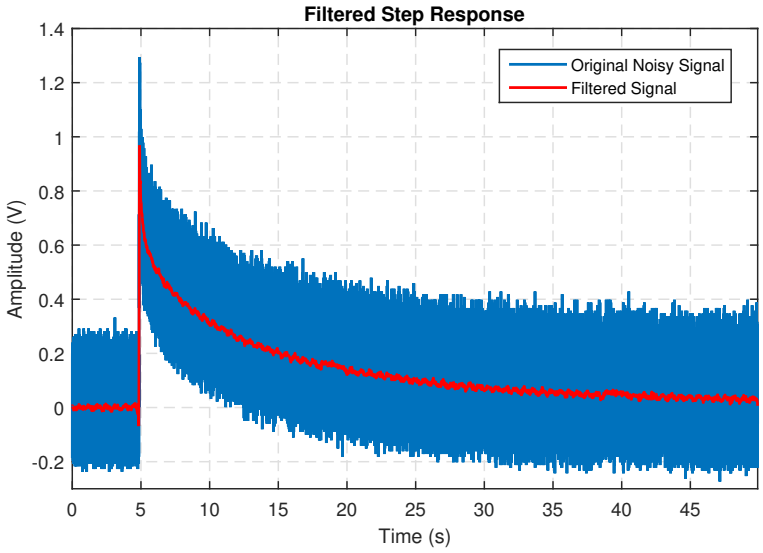

Figure 4.9: Filtered step response and original noisy signal, obtained from one test.

The high gain of the amplification required to read the raw IPMC voltage signal contributed for its weak signal-to-noise ratio. Nevertheless, in future applications, improvements on the signal conditioning circuit are expected to greatly reduce noise power.

From eight tests performed with R_d = 2.7 kΩ, two were rejected due to excessive noise. With the six remaining tests, a statistical mean was calculated. The resulting signal, normalized by the curvature measured during the step test 4.1.1, is shown in figures 4.10 and 4.11. This was later used for model estimation, as described in section 4.1.7.

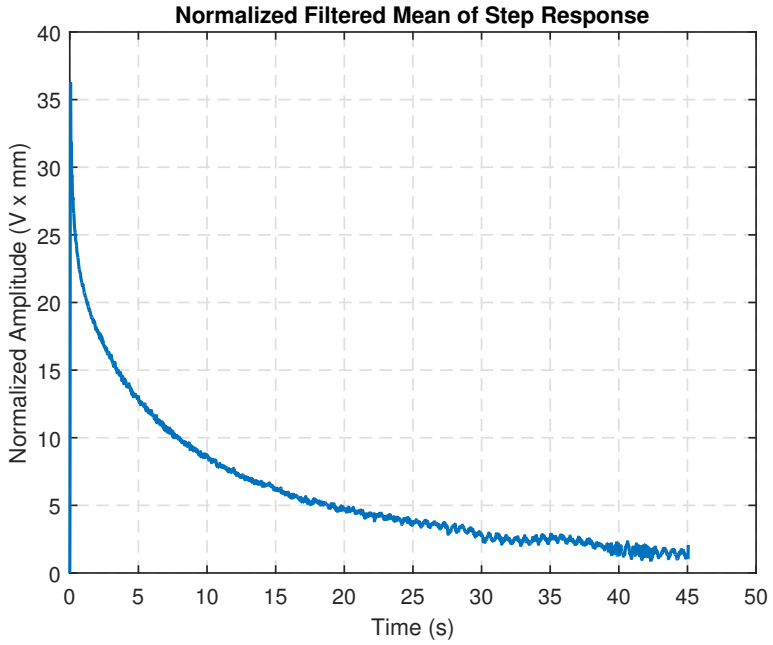

Figure 4.10: Mean step response, filtered and normalized by the curvature. A range of 20 seconds is shown.

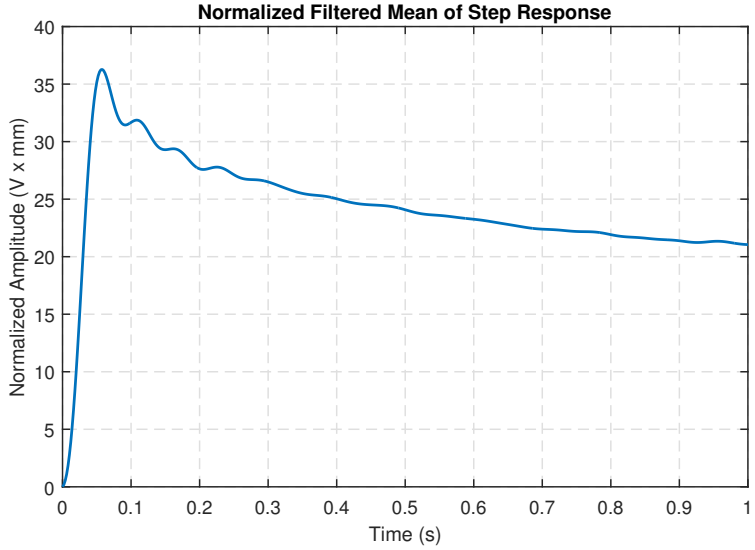

Figure 4.11: Mean step response, filtered and normalized by the curvature. A range of 1 second since actuation is shown.

4.1.7 Modeling Results

From the frequency response results, described in section 4.1.3, a high-pass behavior can be identified in the range of tested frequencies. This can be described by a transfer-function model with at least one zero at reasonably low frequencies, i.e. sufficiently lower than the minimum value tested.

Since the sensor is a true physical system, its transfer function should be strictly proper in order to represent its behavior. This entails a higher number of poles than zeros in the transfer function, so the model should be of at least second order. Nevertheless, if it is assumed that the sensor will only operate within a certain regime (e.g. at limited speeds), a proper transfer function with the same

order of numerator and denominator can be considered for a simplified model. In that case, the simplest transfer function model compatible with the empirical frequency response will be a first-order derivative model:

$$G(s) = \frac{s}{s+a} \tag{4.1}$$

where $s = -a$ is the value of the system pole.

Using a model-fitting tool, a first-order model with relative order zero (the same number of zeros and poles) was fitted to the mean step response result shown in section 4.1.6.

Capturing the first part of the sensor response, where the signal is changing rapidly, was considered more important than its long term variation, for the desired use-case. Also, the sensor should be able to measure static curvature during a short period of time. For these reasons, a range of data comprising 20 seconds, starting at the beginning of the actuation, was used for model estimation.

The resulting model, represented in equation 4.3, achieved a normalized mean-squared error of 79.22 % to the experimental data. A comparison between a step response of the fitted model and the data is shown in figure 4.12.

$$H(s) = \frac{s + 0.1799}{24.87s + 0.8596} \tag{4.2}$$

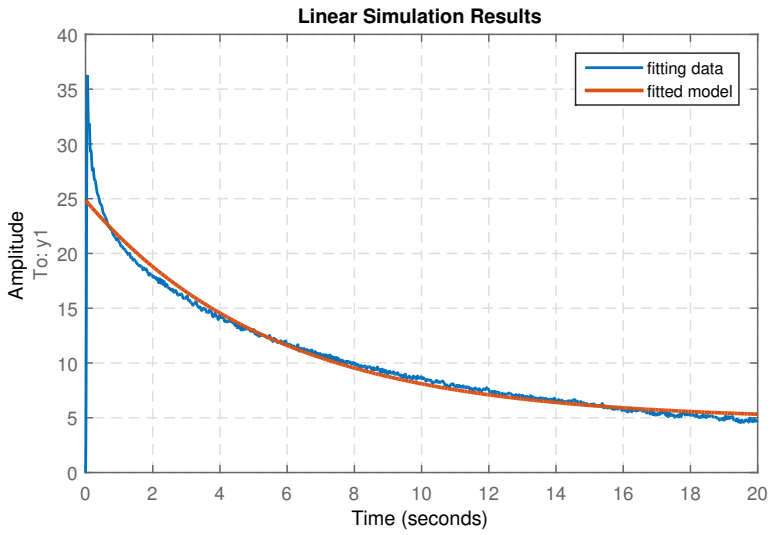

Figure 4.12: Linear simulation of the fitted model with a unit step input, compared to the fitting data.

From figure 4.12, it can be observed that there is a noticeable deviation between the model and the real data in the initial time steps. This was considered acceptable for the intended sensor application, since high-speed dynamics were not very important: as will be seen in the results of section 4.4.2, the inflation of the instrumented actuator prototype did not take less than 1.5 seconds. It should be noted that when fitting the same type of model to different ranges of data, the obtained first-order system models could either approximate the initial voltage decay or the slower decay that is present when a longer time window is used.

To be able to estimate the curvature from the voltage signal given by the sensor, the inverse of the transfer function shown in equation 4.3 was used:

$$J(s) = \frac{1}{H(s)} = \frac{24.87s + 0.8596}{s + 0.1799} \tag{4.3}$$

Since G(s) did not have a non-minimum phase zero or a zero at the origin, J(s) is a stable model. Also, because the G(s) has the same number of zeros and poles, no further modifications were required for ensuring causality.

Validation data corresponding to a step test was used as an input for J(s), in a linear simulation performed in MATLAB®, giving the response represented in figure 4.13.

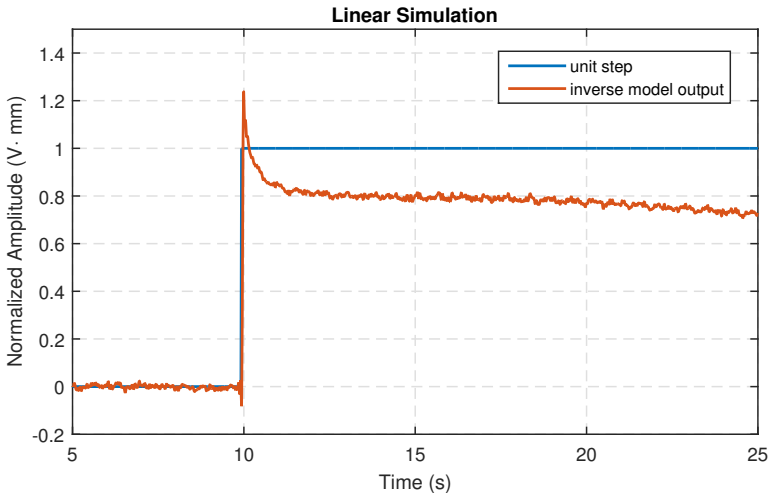

Figure 4.13: Linear simulation of the inverse model, using a normalized sensor response to a step test. A unit step is represented for comparison.

Although the model obtained has the same order of denominator than the physical approximation given in section 2.1, it differs in the order of numerator. In fact, the physical model would not predict the decaying characteristics of the IPMC response obtained in the experiments. This suggests that a dependence of I_{mec} on at least one time derivative of displacement could be added in a future revised model.

4.2 Finite Element Model Validation

4.2.1 Benchmark Actuator Displacement

Using the test bench described in section 3.3.3, the tip displacement of the benchmark actuator was measured in various loading cases. The measured pressure values, presented in table 2.2 were also applied to the finite element model and the homologous displacements were compared to those of the prototype.

Three examples of loading tests and their respective simulation results are depicted in figures 4.14, 4.15 and 4.16, at zero relative pressure, 25,5 kPa and 29,9 kPa, respectively.

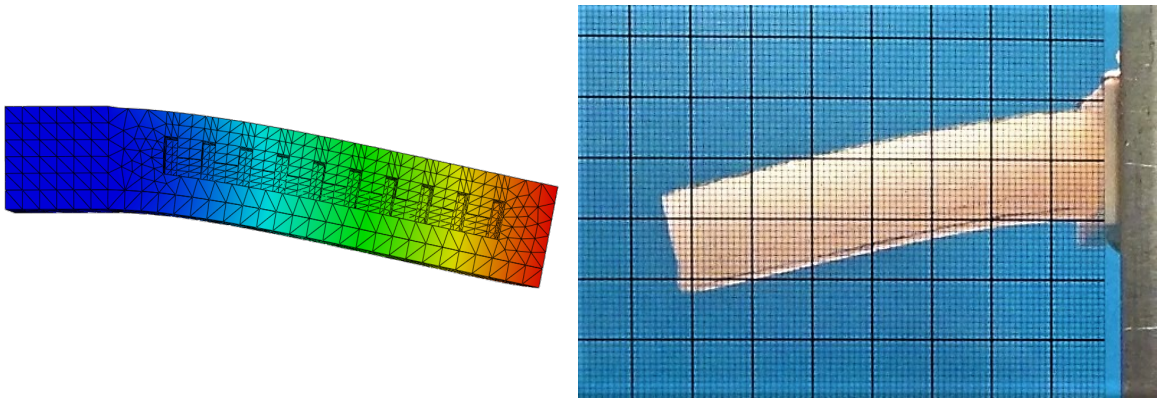

(a) Finite element model **(b)** Benchmark actuator prototype

Figure 4.14: Finite element analysis versus benchmark prototype - gravity load, no pressure applied.

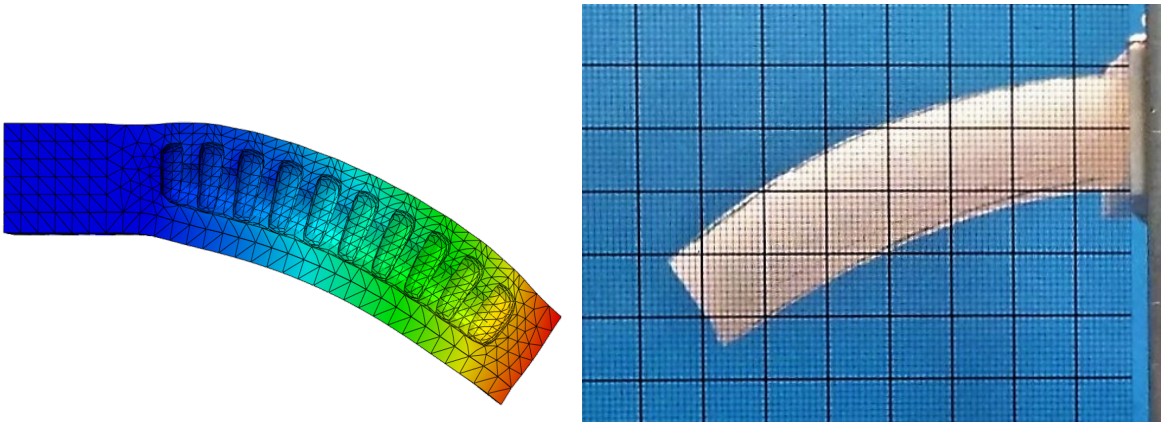

(a) Finite element model **(b)** Benchmark actuator prototype

Figure 4.15: Finite element analysis versus benchmark prototype - gravity load, applied pressure of 25.5 kPa.

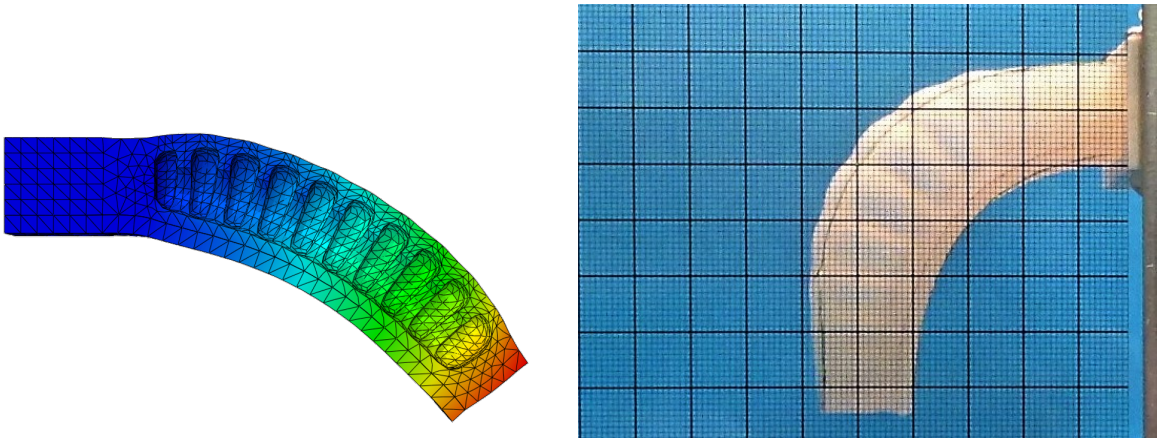

(a) Finite element model **(b)** Benchmark actuator prototype

Figure 4.16: Finite element analysis versus benchmark prototype - gravity load, applied pressure of 29.9 kPa.

The displacement results for the six validation tests performed and corresponding relative error are shown in figure 4.17. An uncertainty of ± 1 mm was assumed in the displacement measurements on the horizontal and vertical axes. This translated to a magnitude uncertainty of $\pm\sqrt{2} \approx \pm 1.41$ mm, represented by the error bars in the figure.

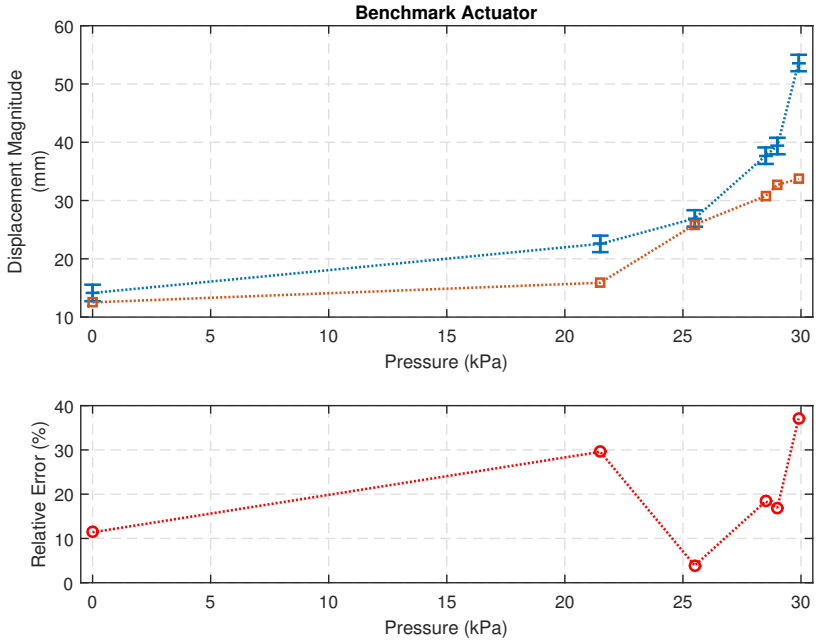

Figure 4.17: Tip displacement under applied pressure: benchmark prototype compared to the finite element model and relative error. The blue error bars represent the uncertainty associated with the prototype displacement measurements.

4.3 Finite Element Analysis of the Instrumented Actuator

4.3.1 Comparison with Benchmark Model

After introducing the IPMC as a superimposed shell mesh with the strip dimensions in the inextensible layer, analyses with the same load conditions as the benchmark model were performed, as described in table 2.2. The IPMC sensor was placed in a region identified as having a regular curvature both in the simulation and the benchmark prototype.

In figure 4.18, the deformed mesh representing the inextensible layer and IPMC is shown, along with the computed Von-Mises stresses, for a pressure of 29.9 kPa in the pneu-net chambers.

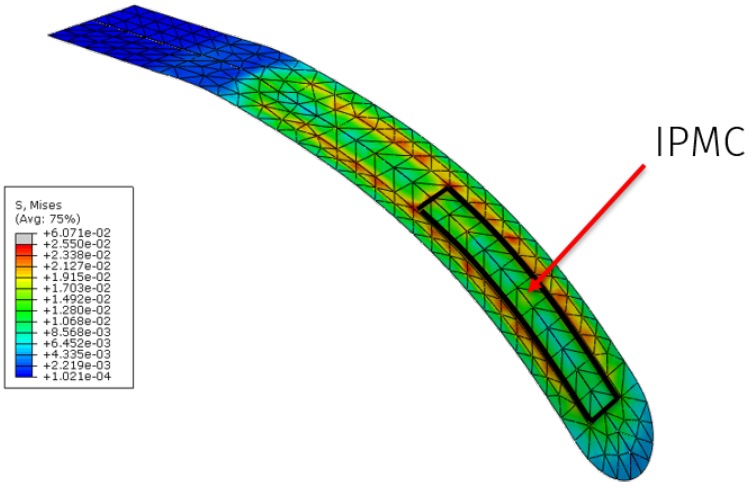

Figure 4.18: Inextensible layer mesh with IPMC in a deformed state, for a chamber pressure of 29.9 kPa.

As can be seen in figure 4.19, the presence of the sensor in the finite element produced a negligible difference in displacement magnitude for the same applied pressure.

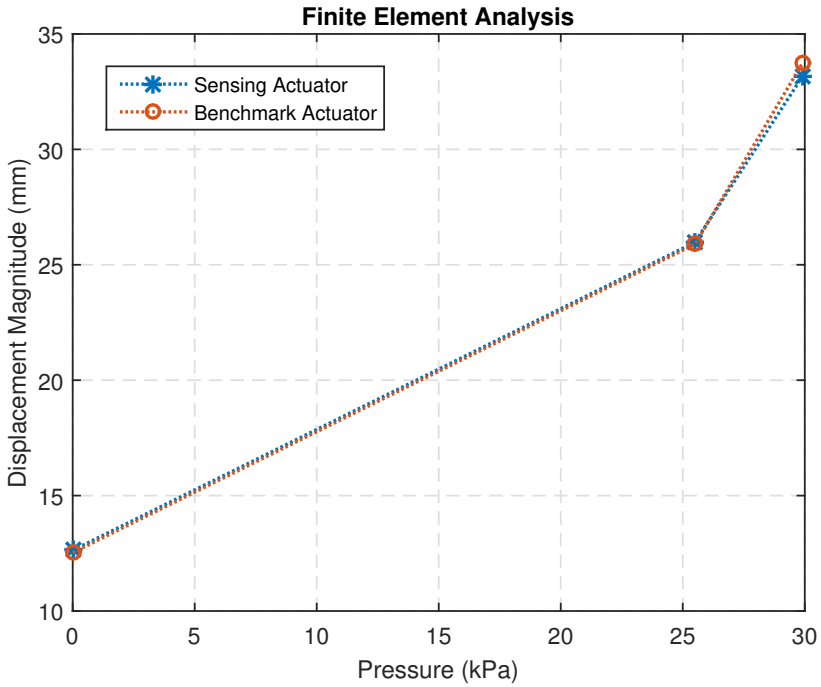

Figure 4.19: Tip displacement under applied pressure: instrumented actuator model compared to the benchmark model.

4.4 Instrumented Pneu-net Prototype Testing

4.4.1 Final Actuator Characteristics

Before soldering the wires joining the two flexible copper contacts on each side of the IPMC sensor, the resistance between them was measured with a multimeter. This allowed for the electrical connections between the platinum layer of the IPMC and the external copper parts to be checked.

On each side of IPMC sensor, the resistance measured between the two contacts before soldering an external wire was found to be less than 50Ω, indicating that a proper electrical connection was established on both sides.

After going through all manufacturing steps, the actuator measured 16 mm in width (not accounting for the sensor wires), 73 m in length and 17 mm in height at the tip.

Due to some present limitations of the manufacturing procedure, the base of the actuator was approximately 1 mm higher than the tip. This caused chambers closest to the base to be slightly bigger and may have also led to a weaker bond between the main body and base layer, in this region. Comparing the prototype to the geometry used for FEA, a height deviation of 1 mm at the tip and 2mm at the base was detected.

When inflating the prototype, a non-uniform deformation was observed. Due to the above problem, the length covered by the IPMC sensor had a much smaller curvature than the base of the actuator, as can be seen in figure 4.20. The base chambers showed a large increase in size, compared to the rest. Such a large difference was not predicted by the finite element model, which approximated the effects of the IPMC strip on the bending stiffness of the inextensible layer.

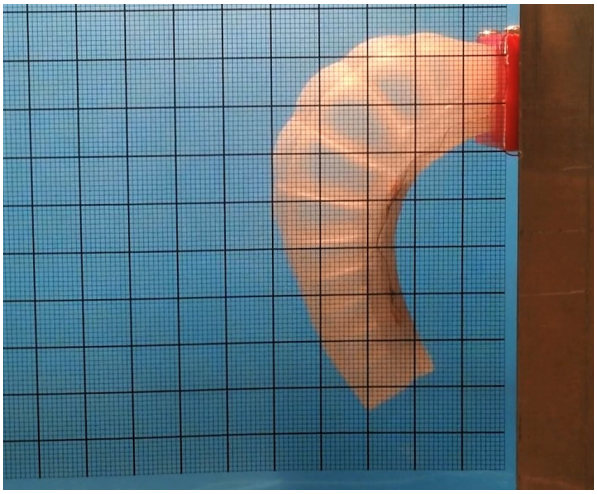

Figure 4.20: Instrumented pneu-net prototype with non-uniform chamber deformation.

Due to the above mentioned anomaly, a small tape band was placed around the affected chambers, to limit their expansion. Since the only curvature of the IPMC sensor was taken into account for the feedback experiments, this intervention is not expected to affect the results.

4.4.2 Feedback Testing

Following the procedure described in section 3.4.4, two inflation/deflation cycles of the instrumented pneu-net prototype were analyzed (figure 4.21).

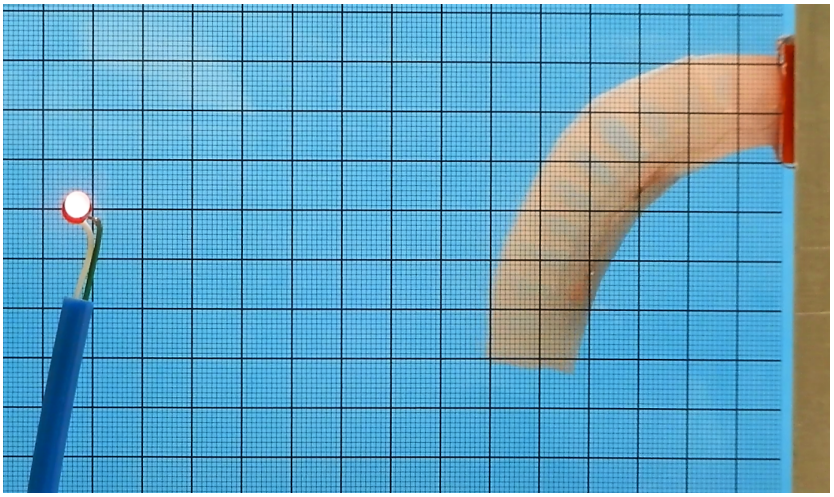

Figure 4.21: Instrumented pneu-net during feedback testing. The red light on the left side was used for signal synchronization.

The voltage signal acquired was filtered offline with a filter similar to that shown in section 4.1.6, but whose passband ended at 1 Hz and stopband started at 2.2 Hz, so as to further smooth the sensor response. The resulting signal, shown in figure 4.22, was then used as an input to a simulation of the inverse model determined in section 4.1.7. The output of the inverse model can be seen in figure 4.23, compared to the curvature measurements taken from the video.

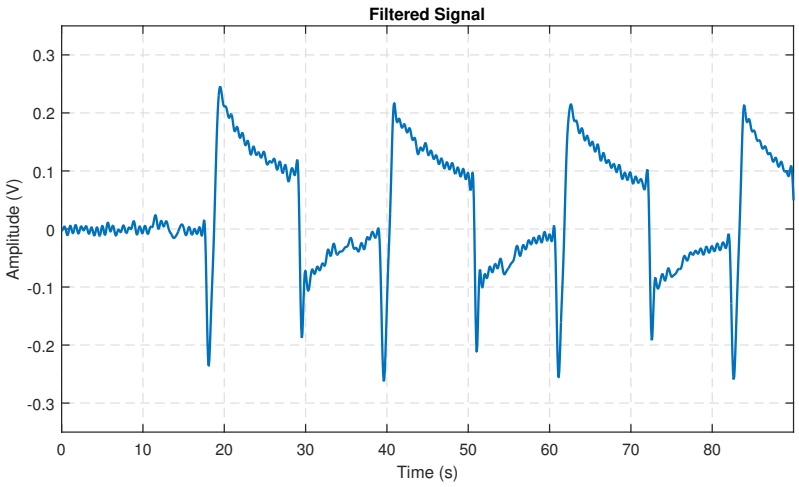

Figure 4.22: Filtered response of the integrated IPMC sensor during a feedback testing cycle.

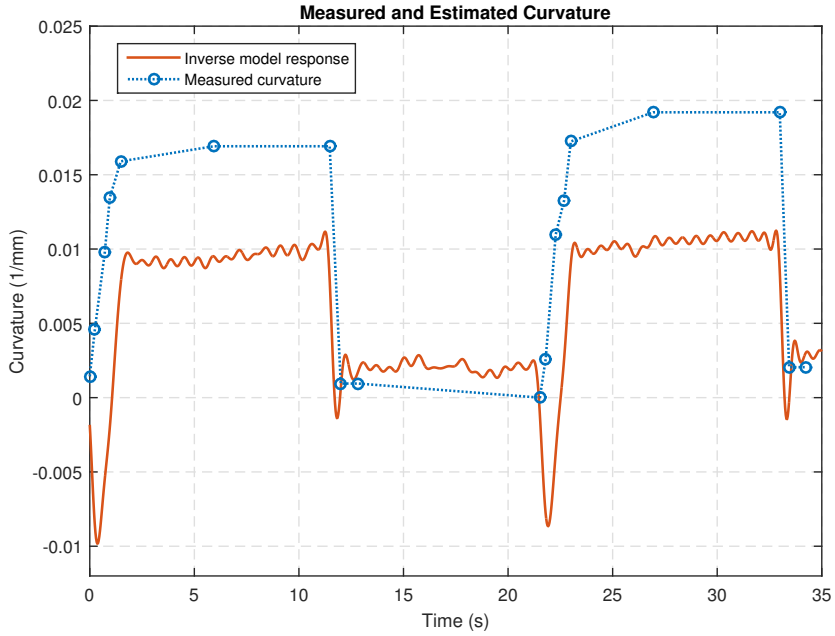

Figure 4.23: Inverse model response and measured actuator curvature.

Subtracting an offset of 0.00133 and multiplying the model output by a recalibration factor of 2.02, the curvature estimated from the sensor readings can more closely match the directly measured values, as shown in figure 4.24.

Figure 4.24: Calibrated inverse model response and measured actuator curvature.

Large negative spikes were observed in the voltage and the resulting curvature signal, during the beginning of each inflation (figures 4.22 and 4.24). This behavior had not been detected during the oscillation and step tests, previously performed with encapsulated IPMC samples. As such, it is expected to have been caused by the specific deformation characteristics of the pneu-net structure

during inflation, as well as possible electrical contact issues.

As predicted by the finite element model (figure 4.18), the inflation of the air chambers caused the cross-section of the actuator to circularize, slightly bending the IPMC in a transversal direction. The resulting transversal curvature had an opposite sign to that imposed along its length during actuation. Since axial bending was still very small in the beginning of the inflation, the transversal curvature could be causing the voltage signal to drop.

5

Conclusions and Future Work

5.1 Conclusions

Having discussed the relevant data from the experiments performed, conclusions about the obtained values are presented in this chapter, along with its practical applications. The developed prototypes also allowed for an empirical evaluation of the theoretical ideas behind its conception, which will be analyzed. General remarks on the limitations found in the methods used are also presented.

A novel encapsulation method was successfully implemented in various IPMC strips and used in continuous bending conditions over extended periods, without any noticeable performance reductions over time.

It was found that an electrolyte with 15 g/l of lithium salt concentration produced the highest amplitude in the sensor output from all of the tested concentrations, clearly improving the IPMC performance upon a configuration without electrolyte. Also, results with this electrolyte presented considerably less variation than with the other concentrations.

Contrary to what was initially expected, electrolyte concentrations of 5 g/l, 25 g/l and 35 g/l did not improve the performance of the IPMC sensor, and added reliability problems.

For the best sensor configuration, a simple linear model was estimated and used for interpreting the sensor response. It was shown that this model could sufficiently describe the dynamic response of the IPMC sample, as long as its high-speed dynamics were neglected and short enough intervals between actuations were considered (i.e. in the range of 20 seconds).

A soft pneu-net actuator was modeled in its original form and with the addition of an IPMC sensor, through finite element analyses, and a very small difference was found between the deformation of both actuators in response to applied pressure. Nevertheless, significant differences were detected between the models and the real prototypes, especially for large displacements. This suggests a more

detailed model may be needed, taking into account the effects of the air inlet in the soft structure and modeling the strain-limiting material more accurately. Also, for ensuring the real actuators closely match its design characteristics, some limitations in the present manufacturing method need to be overcome.

Although some problems were still detected in manufacturing, solutions developed for improving the manufacturing tolerances of pneu-net actuators proved successful - a more uniform chamber wall thickness and more precise textile layer positioning were achieved, when compared to the original manufacturing methods.

Finally, an initial attempt at measuring the curvature of a pneu-net actuator through an integrated IPMC sensor, in conjunction with the aforementioned model, proved successful. However, the band-pass behavior of the IPMC made it difficult not to accumulate error in conditions where slow movements and long duration static bending were prevailing. In cases where only cyclic or fast transient bending is to be detected, the tests performed showed that this sensor was a suitable solution.

It can therefore be concluded that, while the work developed was still an initial approach, the concept of a pneu-net actuator with an embedded IPMC sensor was proven to be feasible, in spite of its limitations.

5.2 Future Work

Possible improvements upon the work developed in the scope of this dissertation, as well as new directions on which to explore the application of IPMC sensors on soft pneumatic actuators are described as follows:

- Further tests for electrolyte comparison - test intermediate concentrations and check if the predicted trend holds.
- Introduce IPMC sensors in different sections of the actuator, to allow for chamber inflation feedback and possibly collision detection.
- Study the effects of reducing the IPMC size
- Explore using the IPMC material as the strain-limiting material, giving it a double purpose - as a structural element and as a sensor.
- Combine the readings of the IPMC output with surface resistance measurements on one side, possibly improving quasi-static operation feedback by using sensor fusion techniques.
- Explore the anisotropic properties of a textile mesh to reinforce the pneu-net chamber walls, for a more efficient actuator.
- Implement a position controller for the developed pneu-net actuator system.

Bibliography

[1] S. Sanan, “Soft Inflatable Robots for Safe Physical Human Interaction,” Ph.D. dissertation, Carnegie Mellon University, 2013.

[2] E. Brown, N. Rodenberg, J. Amend, a. Mozeika, E. Steltz, M. R. Zakin, H. Lipson, and H. M. Jaeger, “From the Cover: Universal robotic gripper based on the jamming of granular material,” *Proceedings of the National Academy of Sciences*, vol. 107, no. 44, pp. 18 809–18 814, 2010.

[3] C. Zheng, S. Shatara, and T. Xiaobo, “Modeling of Biomimetic Robotic Fish Propelled by An Ionic Polymer–Metal Composite Caudal Fin,” *IEEE Transactions on Mechatronics*, vol. 15, no. 3, pp. 448–459, 2010.

[4] T. Li, G. Li, Y. Liang, T. Cheng, J. Dai, X. Yang, and B. Liu, “Fast-moving soft electronic fish,” *Science Advances*, vol. 3, no. 4, pp. 1–8, 2017.

[5] R. V. Martinez, J. L. Branch, C. R. Fish, L. Jin, R. F. Shepherd, R. M. D. Nunes, Z. Suo, and G. M. Whitesides, “Robotic tentacles with three-dimensional mobility based on flexible elastomers,” *Advanced Materials*, vol. 25, no. 2, pp. 205–212, 2013.

[6] F. Ilievski, A. D. Mazzeo, R. F. Shepherd, X. Chen, and G. M. Whitesides, “Soft robotics for chemists,” *Angewandte Chemie - International Edition*, vol. 50, no. 8, pp. 1890–1895, 2011.

[7] M. T. Tolley, R. F. Shepherd, B. Mosadegh, K. C. Galloway, M. Wehner, M. Karpelson, R. J. Wood, and G. M. Whitesides, “A Resilient, Untethered Soft Robot,” *Soft Robotics*, vol. 1, no. 3, pp. 213–223, 2014. [Online]. Available: http://dx.doi.org/10.1089/soro.2014.0008

[8] J. Of, P. E.-j. D. Cherry, and J. F. Wilson, “Fluid actuated limb,” 1988. [Online]. Available: https://www.google.com/patents/US4792173

[9] J. Wilson and I. Norio, “Bellows-type Springs for Robotics,” in *Proc. Adv. Spring Technol. JSSE 60th Anniversary Int. Symp.*, 2007, pp. 109–119. [Online]. Available: http://www.soc.nii.ac.jp/jssr/english/Proceeding/paper15.pdf

[10] R. Hoggett, “1984 - Bellows Robotic Arm/Trunk - James Wilson (American).” [Online]. Available: http://cyberneticzoo.com/bionics/1984-bellows-robotic-armtrunk-james-wilson-american/

[11] Y. Sun, Y. S. Song, and J. Paik, “Characterization of silicone rubber based soft pneumatic actuators,” in *IEEE International Conference on Intelligent Robots and Systems*, 2013, pp. 4446–4453.

[12] B. Mosadegh, P. Polygerinos, C. Keplinger, S. Wennstedt, R. F. Shepherd, U. Gupta, J. Shim, K. Bertoldi, C. J. Walsh, and G. M. Whitesides, "Pneumatic networks for soft robotics that actuate rapidly," *Advanced Functional Materials*, vol. 24, no. 15, pp. 2163–2170, 2014.

[13] L. Paez, G. Agarwal, and J. Paik, "Design and Analysis of a Soft Pneumatic Actuator with Origami Shell Reinforcement," *Soft Robotics*, vol. 3, no. 3, pp. 109–119, 2016.

[14] K. C. Galloway, P. Polygerinos, C. J. Walsh, and R. J. Wood, "Mechanically programmable bend radius for fiber-reinforced soft actuators," *16th International Conference on Advanced Robotics, ICAR 2013*, 2013.

[15] Y. Bar-cohen, *Electroactive Polymer (EAP) Actuators as Artificial Muscles: Reality, Potential, and Challenges, Second Edition*. SPIE Press, ch. 1.

[16] B. Bhandari, G. Y. Lee, and S. H. Ahn, "A review on IPMC material as actuators and sensors: Fabrications, characteristics and applications," *International Journal of Precision Engineering and Manufacturing*, vol. 13, no. 1, pp. 141–163, 2012.

[17] S. J. Peighambardoust, S. Rowshanzamir, and M. Amjadi, *Review of the proton exchange membranes for fuel cell applications*. Elsevier, 2010, vol. 35, no. 17. [Online]. Available: http://dx.doi.org/10.1016/j.ijhydene.2010.05.017

[18] U. Johanson, U. Mäeorg, V. Sammelselg, D. Brandell, A. Punning, M. Kruusmaa, and A. Aabloo, "Electrode reactions in Cu-Pt coated ionic polymer actuators," *Sensors and Actuators, B: Chemical*, vol. 131, no. 1, pp. 340–346, 2008.

[19] S. Nemat-nasser and Y. Wu, "Comparative experimental study of ionic polymer – metal composites with different backbone ionomers and in various cation forms with different backbone ionomers and in various cation forms," *Journal of Applied Physics*, vol. 93, no. 9, pp. 5255–5267, 2003.

[20] P. J. C. Branco, "Uso de Materiais Eletroactivos Iónicos-IPMC na Realização de Sistemas Eletromecânicos: Realidade e Desafios." Instituto Superior Técnico, 2012.

[21] S. Tadokoro, S. Yamagami, T. Takamori, and K. Oguro, "An actuator model of ICPF for robotic applications on the basis of physicochemical hypotheses," in *Proceedings 2000 ICRA. Millennium Conference. IEEE International Conference on Robotics and Automation. Symposia Proceedings (Cat. No.00CH37065)*, vol. 2, 2000, pp. 1340–1346 vol.2.

[22] P. G. de Gennes, K. Okumura, M. Shahinpoor, and K. J. Kim, "Mechanoelectric effects in ionic gels," *EPL (Europhysics Letters)*, vol. 50, no. 4, p. 513, 2000. [Online]. Available: http://stacks.iop.org/0295-5075/50/i=4/a=513

[23] M. Shahinpoor and K. J. Kim, "Ionic polymer-metal composites: I. Fundamentals," *Smart Materials and Structures*, vol. 10, no. 4, p. 819, 2001. [Online]. Available: http://stacks.iop.org/0964-1726/10/i=4/a=327

[24] M. Shahinpoor and K. J. Kim, “Effects of counter-ions on the performance of IPMCs,” in *Proceedings of SPIE*, vol. 3987. SPIE Press, 2000, pp. 110–120. [Online]. Available: http://dx.doi.org/10.1117/12.387769

[25] M. Shahinpoor, “Microelectro-mechanics of ionic polymeric gels as artificial muscles for robotic applications,” in *Proceedings IEEE International Conference on Robotics and Automation*, 1993, pp. 380–385 vol.2.

[26] S. Tadokoro, S. Yamagami, T. Takamori, and K. Oguro, “Modeling of Nafion-Pt composite actuators (ICPF) by ionic motion,” in *Proceedings of SPIE*, vol. 3987. SPIE Press, 2000, pp. 92–102. [Online]. Available: http://dx.doi.org/10.1117/12.387767

[27] S. Nemat-Nasser and J. Y. Li, “Electromechanical response of ionic polymer-metal composites,” *Journal of Applied Physics*, vol. 87, no. 7, p. 3321, 2000. [Online]. Available: http://scitation.aip.org/content/aip/journal/jap/87/7/10.1063/1.372343

[28] S. Nemat-Nasser, “Micromechanics of actuation of ionic polymer-metal composites,” *Journal of Applied Physics*, vol. 92, no. 5, pp. 2899–2915, 2002.

[29] P. J. C. Branco and J. A. Dente, “Derivation of a continuum model and its electric equivalent-circuit representation for ionic polymer–metal composite (IPMC) electromechanics,” *Smart Materials and Structures*, vol. 15, no. 2, pp. 378–392, 2006.

[30] J. C. Case, E. L. White, and R. K. Kramer, “Soft Material Characterization for Robotic Applications,” *Soft Robotics*, vol. 2, no. 2, pp. 80–87, 2015. [Online]. Available: http://online.liebertpub.com/doi/10.1089/soro.2015.0002

[31] G. Agarwal, N. Besuchet, B. Audergon, and J. Paik, “Stretchable Materials for Robust Soft Actuators towards Assistive Wearable Devices,” *Scientific Reports*, vol. 6, no. September, p. 34224, 2016. [Online]. Available: http://dx.doi.org/10.1038/srep34224http://www.nature.com/articles/srep34224

[32] P. Polygerinos, B. Mosadegh, and A. Campo, “PneuNets Bending Actuators.” [Online]. Available: http://softroboticstoolkit.com/book/pneunets-bending-actuator

[33] J. Barramba, J. Silva, and P. J. Costa Branco, “Evaluation of dielectric gel coating for encapsulation of ionic polymer-metal composite (IPMC) actuators,” *Sensors and Actuators, A: Physical*, vol. 140, no. 2, pp. 232–238, 2007.

[34] B. Lopes and P. J. Costa Branco, “Ionic polymer metal-composite (IPMC) actuators: Augmentation of their actuation force capability,” *IECON Proceedings (Industrial Electronics Conference)*, pp. 1180–1184, 2009.

[35] C. Lim, H. Lei, and X. Tan, “Characterization and modeling of humidity-dependence of IPMC sensing dynamics,” in *Proceedings of SPIE*, vol. 8687, 2013, pp. 868 710–868 720. [Online]. Available: http://dx.doi.org/10.1117/12.2010612

[36] L. Lourenço, “Caracterização do Armazenamento de Energia Eléctrica em Materiais Electroactivos IPMC: Condensadores Flexíveis,” Master’s thesis, Instituto Superior Técnico, 2012.

A

Additional Test Results

Additional oscillation tests were performed with a type 2 encapsulation, in order to find if the dispersion of the results could be reduced by changing the encapsulation. Electrolytes with two lithium salt concentrations were used: 15 g/l and 35 g/l (figures A.1 and A.2. An additional IPMC sample was tested without electrolyte (figure A.3).

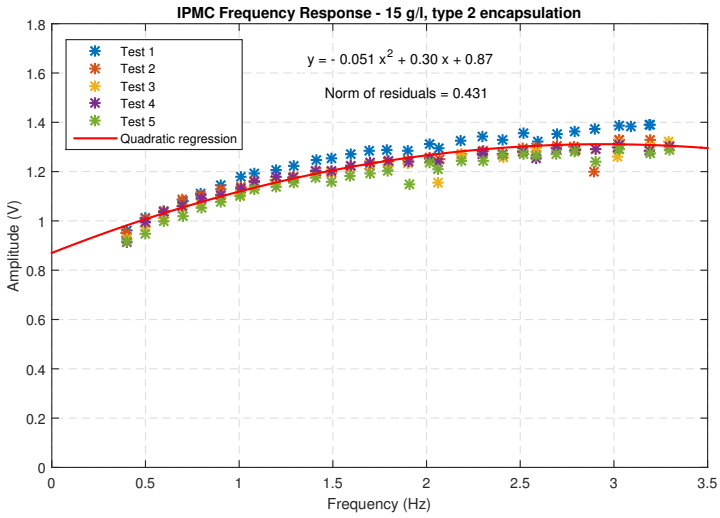

Figure A.1: Oscillation test results and fitted polynomial for an IPMC sample with a 15 g/l electrolyte, using a type 2 encapsulation.

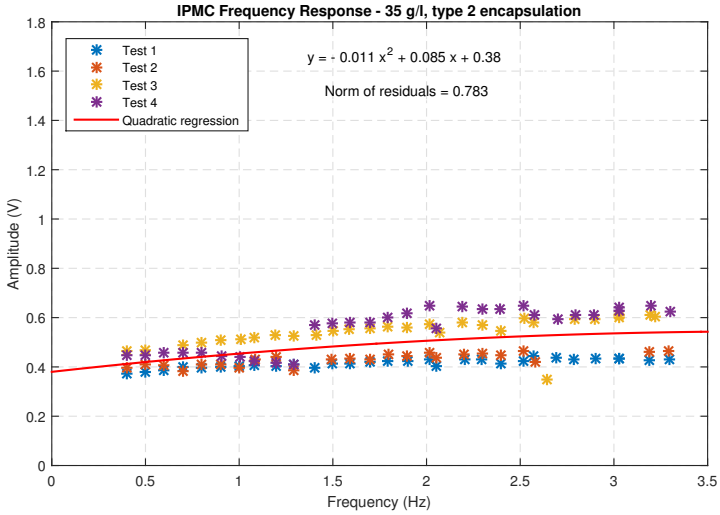

Figure A.2: Oscillation test results and fitted polynomial for an IPMC sample with a 35 g/l electrolyte, using a type 2 encapsulation.

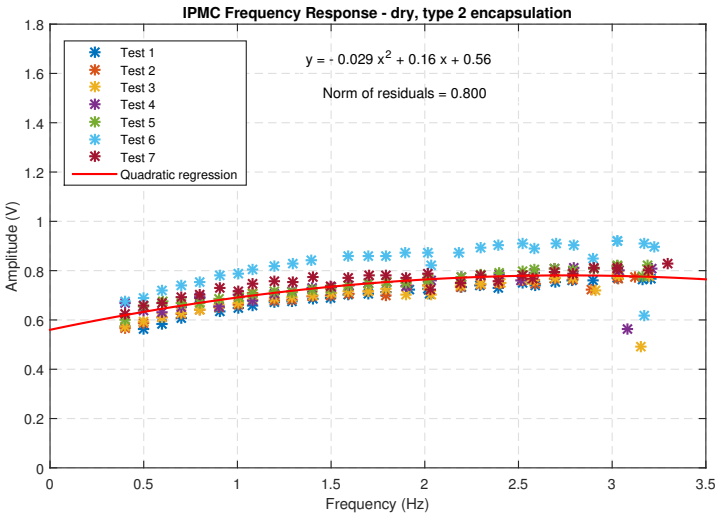

Figure A.3: Oscillation test results and fitted polynomial for an IPMC sample without electrolyte, using a type 2 encapsulation.

It can be observed that the dispersion of the new results obtained using electrolyte was much lower than that obtained with the type 1 encapsulation. On the other hand, the results obtained without electrolyte did not show any reduction in the dispersion.